

1-1-2015

Characterization of Groundwater Discharge in a Back Barrier Tidal Creek

Matthew L. Carter
Coastal Carolina University

Follow this and additional works at: <https://digitalcommons.coastal.edu/etd>

 Part of the [Hydrology Commons](#)

Recommended Citation

Carter, Matthew L., "Characterization of Groundwater Discharge in a Back Barrier Tidal Creek" (2015). *Electronic Theses and Dissertations*. 7.
<https://digitalcommons.coastal.edu/etd/7>

This Thesis is brought to you for free and open access by the College of Graduate Studies and Research at CCU Digital Commons. It has been accepted for inclusion in Electronic Theses and Dissertations by an authorized administrator of CCU Digital Commons. For more information, please contact commons@coastal.edu.

**Characterization of groundwater discharge in a back barrier
tidal creek**

Matthew L. Carter

Submitted in Partial Fulfillment of the
Requirements for the Degree of Master of Science in
Coastal Marine and Wetland Studies in the
College of Science
Coastal Carolina University
2015

Dr. Richard F. Viso

Dr. Richard N. Peterson

Dr. Jenna C. Hill

Dr. Christof Meile

ACKNOWLEDGEMENTS

I would like to express my utmost gratitude to my thesis committee, Dr. Rich Viso, Dr. Rick Peterson, Dr. Jenna Hill and Dr. Christof Meile. Foremost, I would like to thank my primary advisor, Rich, for his continuous support of my M.S. study and research, for his character, motivation, enthusiasm and immense knowledge. If it weren't for Rich, I would have never had this opportunity. I extend a special thanks to Dr. Rick Peterson, for his mentoring and, guidance throughout the course of my degree.

I greatly appreciate the help and support of the Groundwater Discharge Measurement Facility at Coastal Carolina University and friends, for providing resources and all of the hard work during the extended field collection. Bradly Craig, Leigha Peterson, Sarah Chappel, Samantha Maness, and Brittany Hoffnagle, without your help, I may have never accomplished this endeavor.

Lastly, I thank my family for the support and encouragement through the course of my Master's degree. This has been a wonderful experience and I have had a great support from friends, family, and mentors.

Abstract

Groundwater discharge in the coastal environment is known to be a complex process. The driving mechanisms of groundwater discharge vary on spatial and temporal scales that can significantly impact coastal water chemistry and play a role in ecological zonation. Evolving combinations of observational and modeling approaches provide a basis to quantify groundwater discharge in a spatial and temporal sense. Here we employ a combination of geochemical (naturally occurring radon isotope) and geophysical (electrical resistivity) techniques to measure groundwater-surface water interactions along a back-barrier tidal creek. In addition to field measurements, a unique non-steady state radon mass balance equation was developed to better constrain groundwater estimates. The radon mass balance shows spatial and temporal variance in groundwater composition along the tidal creek. Our estimates suggest that groundwater discharge is greater in the Upper Duplin compared to the Lower Duplin section. Spring tide conditions yielded greater groundwater discharge at all sites, but the Lower Duplin section had significantly greater discharge when compared to neap tide discharge. Electrical resistivity serves as a qualitative assessment to support the radon mass balance findings of marsh zone water circulation on both daily and spring/neap cycles. Our observations proved baseline groundwater contributions to the Duplin River system. This can be used to constrain aquifer characteristic used in numerical simulations of chemical and nutrient transport the systems.

TABLE OF CONTENTS

ACKNOWLEDGEMENTS	i
ABSTRACT	ii
TABLE OF CONTENTS	iii
LIST OF TABLES	iv
LIST OF FIGURES	v
INTRODUCTION	1
Site Description	3
METHODS	6
Field Measurements: Radon-222	7
Radon Mass Balance	8
Field Measurements: Electrical Resistivity	15
RESULTS	17
Field Measurements	17
Groundwater Endmembers	18
Groundwater Discharge Model	19
Electrical Resistivity	20
DISCUSSION	21
Radon Mass Balance	21
Electrical Resistivity	25
Groundwater dynamics	28
CONCLUSIONS	31
LITERATURE CITED	33
TABLES	45
FIGURES	48
APEPENDIX A	65
APEPENDIX B	72
APEPENDIX C	93

LIST OF TABLES

Table 1: Results of the marsh sediment equilibration measurements arranged by depth profiles. Radon-222 measurement errors represent 1- σ uncertainties.

Table 2: Summary of the sensitivity analysis of individual parameter influence on groundwater discharge values. Individual parameters were altered 10% and input into the radon mass balance equation for analysis. * indicates a parameter has a significant role in the groundwater discharge value.

Table 3: Surface area coverage of spring and neap conditions for the various Duplin River sections. Surface areas shown are the average tidal amplitude during the spring and neap conditions. The percent change reflects the increase in section surface area compared during spring tide compared to neap tide.

LIST OF FIGURES

Figure 1: Location of the study site on Sapelo Island, Georgia. The main panel is a digital elevation model of the Duplin River catchment (outline in Black). Inserts show time series radon stations (white circles) and resistivity transects (yellow lines) at Upper Duplin (A), Central Duplin (B), and Lower Duplin (C) stations.

Figure 2: Conceptual model of our 3-box radon mass balance model. The dashed line between the boxes indicates the position of our radon time series stations and defines the dimensions of each river section. The arrows represent the flow of water (and therefore radon) into and out of each box during flood tide (A) and ebb tide (B).

Figure 3: Time series graphs of the field parameters collected during the study. Surface water radon activity for Upper Duplin (A), Central Duplin (B), Lower Duplin (C), water levels from Upper Duplin (representative of tidal characteristics; D), wind speeds (E) and precipitation (F) are shown for our June 2013 observations.

Figure 4: Observed radon activities from the three measurement stations (30 minute interval measurements). Box plots show median values (solid horizontal line), mean (dashed line), 50th percentile values (box outline), 10th and 90th percentile values (whiskers), and 5th/95th outlier values (black circles).

Figure 5: Radon activities at the Upper Duplin site shows an inverse correlation with water level. High radon activities occur during low water levels, and low radon activity during high water levels.

Figure 6: Average daily radon activities during the deployment in relation to the tidal trends of the Duplin River.

Figure 7: Time series salinity measurements from Upper Duplin, Central Duplin, and Lower Duplin (A). Salinity and water level are compared from the Upper Duplin station under neap (B) and spring (C) tidal conditions. Note the salinity reversal on 6/23 that occurs only at Upper Duplin (C).

Figure 8: 30-minute interval groundwater discharge rates from the non-steady state mass balance equation at Upper Duplin (A), Central Duplin (B), and Lower Duplin (C).

Figure 9: Total groundwater discharge from each river section over a 12 hour tidal cycle (black bars) and surface water discharge (gray bars) at Upper Duplin (A) Central Duplin (B) Lower Duplin (C). Percent groundwater composition of discharging water is shown by the line graph.

Figure 10: Total 12-hour groundwater discharge normalized to length of main channel in each section for the measurement duration (A) neap tide conditions (B) and spring tide conditions (C). Box plots show median values (solid horizontal line), mean (dashed line), 50th percentile values (box outline), 10th and 90th percentile values (whiskers), and individual outlier values (black circles).

Figure 11: Stationary time series resistivity tomograms across a marsh platform at the Upper Duplin site as a function of water level.

Figure 12: Time series resistivity tomograms across the marsh platform at the Central Duplin site as a function of water level.

Figure 13: 30-minute interval groundwater discharge at the Upper Duplin site (red bars) corresponding to tidal stage (black lines). Maximum groundwater discharge occurs during peak tide flow.

Figure 14: 30-minute groundwater discharge rate calculated from the steady-state mass balance equation for the Upper (A), Central (B), and Lower (C) Duplin sections.

Figure 15: Comparison of the 12-hour groundwater discharge totals between the steady-state mass balance approach (y-axis) and our non-steady state mass balance approach (x-axis).

Figure 16: Upper Duplin (top) and Central Duplin (bottom) resistivity tomograms for both spring and neap time series measurements. The warm colors (red and orange) indicate higher values of resistivity signifying freshening of porewater, while cool colors (blue) indicates lower resistivity values indicating salt-water intrusion.

1. Introduction:

Constraining processes that control exchange of dissolved materials between land and sea is essential to understanding coastal ecosystems. The complexity of dynamic coastal environments limits the ability to achieve complete and detailed understanding of biogeochemical cycling (Valiela et al., 1978; Johannes, 1980). One important process controlling material cycling in this setting is submarine groundwater discharge (SGD), defined as the discharge of groundwater across the sediment-water interface into estuaries, bays, and oceans regardless of fluid composition or driving force (Burnett et al., 2006). Over the last few decades, groundwater discharge has been identified as a significant transport mechanism for terrestrially derived macro- and micro- nutrients, as well as products of diagenesis to surface waters that may positively or negatively impact an ecosystem (Johannes, 1980; Taniguchi et al., 2002; Slomp and Van Cappellen, 2004; Zhang and Mandal, 2012). Particularly within coastal ecosystems, the vast array of landforms, geological types (organic-rich mud, sands, carbonate) and coastal processes (waves, tides, etc.) complicate efforts to fully characterize SGD across the range of applicable spatial and temporal scales (Burnett et al., 2006; Santos et al., 2012).

Ever evolving combinations of observational and modeling approaches provide a basis to quantify the various material sources and sinks spanning the land-sea boundary. Direct observations such as seepage meters provide excellent details about localized SGD characteristics, but generally fail to represent spatial variability (Taniguchi et al., 2003). In rapidly changing coastal environments, time series measurement stations at multiple locations are necessary to accurately estimate SGD, but are difficult to maintain (Santos and Eyre, 2011; Makings et al., 2014; Tait et al., 2013). Numerical simulations provide a

basis for exploring the SGD processes in response to a broad range of variables; however, these models must be constrained by accurate observational data (Nakada et al., 2011).

Recent approaches to quantify SGD implement measurements of naturally occurring radioisotopes that serve as tracers of groundwater. Radon (Rn-222) is an established proxy for groundwater discharge due to its conservative, non-reactive nature and elevated levels in groundwaters relative to surface waters (see reviews in Burnett et al., 2006; Swarzenski et al., 2007a; Charette et al., 2008). Studies have utilized Rn-222 in different approaches to account for SGD within complex settings with complicated hydrodynamic forces such as tides and riverine inputs (Santos et al., 2008; Peterson et al., 2010; Makings et al., 2014). Time series measurement techniques have led to better estimates of minimum and maximum groundwater discharge rates (Peterson et al., 2010), spatial distribution of groundwater inputs along a river channel (Kim et al., 2010) and the driving forces of SGD (Gleeson et al., 2013).

In an effort to gain a more complete understanding of SGD processes, geochemical tracer methods have been combined with geophysical imaging techniques to support and describe groundwater dynamics. A useful geophysical technique is electrical resistivity profiling (ER). A non-unique measurement method that injects a known current into the subsurface and as the current propagates outward, receiver electrodes measure voltage drops between the injection points and the receivers (Daily et al., 2004). In the last few decades, computer modeling program advancements have greatly increased the utility of ER subsurface imagery (Zhou et al., 2000; Manheim et al., 2004; Burger et al., 2006). Developments of streaming and stationary marine cables with multichannel resistivity meters have generated high-resolution data (Manheim et al.,

2004). The meters have the capability to simultaneously measure multiple channels using a high power transmitter that greatly increases data collection speeds. This system can be useful for studying the freshwater/saltwater interface in a tidally modulated region. In coastal settings, where the “subterranean estuary” described by Moore (1999) contains variable of porewater salinities, electrical resistivity has proven particularly useful in providing qualitative images that help visualize groundwater discharge dynamics (Schultz and Ruppel, 2002; Swarzenski et al., 2006; Schultz et al., 2007; Swarzenski et al., 2007b).

Here we estimate the temporal and spatial influence of groundwater discharge in a large tidal creek, the Duplin River, within an extensive back barrier marsh setting. We present a non-steady state radon mass balance model to quantify groundwater discharge. Our model accounts for volumetric change in the river as a function of water level variations and inundated bathymetry as a basis to constrain groundwater discharge calculations. In addition, electrical resistivity tomography depicts changes in time-lapse images as evidence of tidal processes controlling groundwater discharge variability, as well as hydrogeological differences between localized sub-regions within the larger study area. The combination of time series geochemical and geophysical techniques advances our understanding of the driving processes that control temporal and spatial variability in groundwater discharge within this salt marsh ecosystem.

1.2 Site Description:

Located along the South Atlantic Bight, the Georgia coastline is characterized by a 160 km stretch of complex primary and secondary barrier islands resulting from

processes associated with long-term sea level change, accretion, seasonal tidal events, storm over-wash, and wave-driven erosion (Hoyt, 1967; Johnson and Barbour, 1990). Sapelo Island is one such barrier island in this area that is separated from the mainland by extensive back barrier salt marsh and tidal creeks that regulate water flow to and from the coastal ocean. The island consists of late Pleistocene and early Tertiary well-sorted, fine sands with a clay layer ranging 4-30 m thick with average clay layer depth of 12 meters (Schultz and Ruppel, 2002). Holocene beach sand deposits outline the seaward side of the island. The adjoining marshes consist of silts and clays with some fine Holocene sands and reworked Pleistocene mud.

Sapelo Island, GA is part of the NSF supported Long-Term Ecological Research (LTER) program. The LTER is dedicated to monitoring long term impacts to diverse ecosystems across the country. The Georgia Coastal Ecosystems-LTER was established in 2000 as a study domain to understand patterns and processes that shape complex estuarine habitats. Monitoring the habitat on a multitude of spatial and temporal scales leads to the identification of long-term trends caused by climate change, sea level rise, and anthropogenic interactions. Within the GCE-LTER domain, the Duplin River is a well-studied location that serves as a platform for interdisciplinary research to progress a holistic approach to understanding the ecosystem.

The Duplin River is oriented roughly north-south and separates Sapelo Island from the mainland (Figure 1). The Duplin River is a large tidal creek, 12.5 km in length with a catchment of $1.66 \times 10^6 \text{ m}^2$ during mean low water (MLW) that connect to the Atlantic Ocean through Dobby Sound in the south and terminates in the salt marsh to the north (Ragotzki and Bryson, 1955). The marsh system is dominated by *Spartina* salt

marsh with a few elevated wooded barrier island remnants known as hammocks. The river channel ranges from 100-300 m wide in the lower stretches to only a few meters wide at the headwaters. The average tidal range is between 1.2 – 2.5 m with a spring high of 3.4 m (Ragotzki and Bryson, 1955). Previous hydrological and bed-form morphology studies have shown the Duplin River to be an ebb-dominated system (Kjerfve, 1973; Zarillo, 1982; Zarillo, 1985).

The only freshwater contributions to the system are from direct precipitation, and fresh groundwater, yet the salinity ranges 15-33 psu along the Duplin River (Kjerfve, 1973). The lower reaches near Doboy Sound have significant tidally-driven salinity variation owing to advection of fresh water from the nearby Altamaha River discharge (Di Iorio and Castelao, 2013). The middle and upper reaches have minimal tidally-driven variability in salinity (Kjerfve, 1973; McKay and Di Iorio, 2010). McKay and Di Iorio (2010) have shown the total salt fluxes in the Duplin River pulse at the spring-neap tidal frequency, suggesting increased salt accumulation in the mid and upper reaches during neap tide and maximum river discharge at spring tide.

There are three clear morphological differences along the Duplin River channel and the associated salt marshes are typical of various marsh maturation stages (Wadsworth, 1980; Frey and Bason, 1985). The lower Duplin marsh system resembles a mature marsh consisting of table-top salt marsh morphology with a well-developed tidal channel and an exposed marsh cliff reflecting a low drainage density (Wadsworth, 1980). The middle reaches resemble an intermediate age marsh system with a combination of a developing main channel and a few side channels (Wadsworth, 1980; Frey and Bason, 1985). The upper reaches and side channels consist predominantly of tall *Spartina* and a

high drainage density that resembles a dendritic pattern typical of a young marsh system (Wadsworth, 1980). The combination of marsh morphologies can be attributed to the Georgia coastline instability and the limited time for a well-developed marsh system to evolve.

The geophysical case study of Sapelo Island by Schultz et al. (2007) has shown sub-marsh flow paths to be possible conduits for groundwater discharge to tidal creeks. On localized scales (5-25 m horizontal distance) Schultz et al. (2007) show lithological controls impacting vertical interaction between shallow and deeper aquifers. On a fine scale (0.1-2 m) the presence of vertical fingering (convection) was observed within the shallow marsh where driving mechanisms of exchange can be linked to shallow biological and physical conditions (Schultz et al., 2007). Island scale surveys of the surficial freshwater lens demonstrate that seasonal changes in salinity and recharge can influence the large scale environment.

2. Methods:

The magnitude and location of groundwater inputs can be highly variable in back barrier tidal creeks. Our study used a combination of geochemical and geophysical measurements to constrain groundwater inputs to the Duplin River across a full tidal regime. The field deployment took place over a four week period from June 3rd – June 27th, 2013. The geochemical tracer Rn-222 was used in a continuous time series approach as a proxy to estimate groundwater inputs at various tidal stages. Multiple Rn-222 measurement stations along the Duplin River provide information about spatial differences in groundwater inputs. The sampling frequency allows for groundwater input

comparisons between short (daily tides) variability to longer fortnightly (spring/neap) trends. Electrical resistivity profiling was used in conjunction with the geochemical measurements to visualize shallow aquifer dynamics and identify the primary driving forces of groundwater discharge to the Duplin River system.

2.1 Field Measurements: Radon-222

Continuous radon measurements were made from three stations along the Duplin River (Figure 1). Station 1, Lower Duplin was located on a floating dock 0.5 km from the mouth of the Duplin River where it drains to Doboy Sound ($31^{\circ}25'04.10$ N $81^{\circ}17'46.51$ W). Station 2, Central Duplin, was located on a pier in the middle reaches of the river about 5.5 km from the mouth ($31^{\circ}27'35.70''$ N, $81^{\circ}16'38.49''$ W). Station 3, Upper Duplin, was located on a floating dock in the upper reaches of the Duplin River, about 9 km from the mouth ($31^{\circ}28'44.09''$ N, $81^{\circ}16'23.12''$ W). The sites were selected based upon river accessibility for instrument deployment (Figure 1). The instrument deployment stations served as division points for our radon box model to constrain groundwater inputs.

Continuous measurements of dissolved radon-222 were made using an automated sampling approach described by Burnett et al. (2001). Briefly, at each station, a commercial RAD7 radon-in-air monitor (DurrIDGE Co.) was connected via a closed air loop with an air-water exchanger (RAD-AQUA; DurrIDGE Co.). A floating submersible pump continuously supplied river water (~ 1 m below the river surface) to the air-water exchanger allowing radon to equilibrate between gaseous and aqueous phases. The RAD7 measures radon-222 activities via alpha decays of its daughter (Po-218) over 30-

minute intervals. Water level at each station was measured continuously with a HOBO water level logger (Onset Corp.) fixed to the bottom, and water temperature and conductivity were measured via a Solinst LTC Levelogger Junior fixed to the submersible pump.

In December 2013, a total of six shallow sediment cores (~2 meters) were collected in along the Duplin River's intertidal salt marsh using standard vibracore methods (for detailed equipment and methods see: Lanesky et al., 1979; Thompson et al., 1991). Two core samples (near river and upland) were collected along each resistivity transect at the Upper and Central Duplin sites. At the Lower Duplin site, two core samples were collected near the radon time series station (roughly 50 meters and 100 meters from the river channel). The core samples were taken back to the laboratory for grain size and radon end-member analysis.

The sediments were sealed for three weeks in radium free water to allow for Rn-222 to reach secular equilibrium with the particle bound Ra-226. Results of the ingrowth represented the maximum in-water radon activity that can be obtained from groundwater inputs (Corbett et al., 1998).

2.2 Radon Mass Balance:

We used a radon mass balance approach to quantify groundwater fluxes to the Duplin River. This mass balance approach was based on a similar approach developed by Peterson et al. (2010) in a similar river system in Florida. The model by Peterson et al. (2010) was limited to constraining maximum and minimum extents of groundwater fluxing out of the river system because of a lack of well-defined spatial constraints within

their studied system. We improved upon that model by dividing the Duplin River system into discrete boxes (upper, central, and lower reaches). A high-resolution digital elevation model (DEM) of river bathymetry and flood plain elevations allowed us to continuously constrain the surface area and water volume within each box through time based on measured water levels (Blanton et al., 2007).

We considered our radon mass balance differently between flood and ebb tide (Figure 2). During flood tide (Figure 2A), changes in radon mass within each box resulted from a balance between inputs (upstream tidal intrusion, groundwater discharge, and ingrowth from dissolved Ra-226) and outputs (transfer of radon-rich water farther upstream, radioactive decay, and atmospheric degassing resulting from both wind and current evasion). In the uppermost section of the river, we did not consider the transfer of radon-rich water farther upstream as that box encompasses the headwaters of the river system.

Our mass balance equations were modified from a steady-state mass balance approach outlined by Santos et al. (2010). Whereas Santos et al. (2010) assumed steady-state conditions within their study domain (i.e., inputs equal outputs), our high-resolution DEM allowed us to estimate the radon mass within the study domain at each measurement point, and therefore we do not need to assume steady-state conditions. During flood tide, our radon mass balance equation is:

$$\frac{\Delta Rn}{\Delta t} = \{([Rn_{ocean}] \cdot Q_{in}) + ([Rn_{gw}] \cdot Q_{gw}) + ([Ra_{226}] \cdot \lambda_{Rn} \cdot V_{box})\} - \{([Rn_{out}] \cdot Q_{out}) + ([Rn_{box}] \cdot \lambda_{Rn} \cdot V_{box}) + A_{box} \cdot (J_{wind} + J_{current})\} \quad (1)$$

The individual terms here are described in the subsections to follow. In general, terms in brackets (e.g., $[Rn_{ocean}]$) indicate measured concentrations of various parameters, and Q terms indicate water flux rates. This equation is solved separately for each box at 30-minute intervals during flood tide periods. The ebb tide equation is described later.

Change in radon mass in each box with time: $\Delta Rn/\Delta t$

The term $\frac{\Delta Rn \left(\frac{dpm}{m^3} \right)}{\Delta t}$ is identified as total change in Rn-222 activity over time within an individual section. The term is derived by first estimating the total radon activity within a particular box (as the average radon activity measured from the bordering stations) multiplied by the volume of that box during the measurement interval. We then calculate the difference in these values between subsequent measurement cycles. This calculation can be described mathematically as:

$$\Delta Rn = \left(\frac{[Rn_u] + [Rn_d]}{2} \cdot V_{box} \right)_{t2} - \left(\frac{[Rn_u] + [Rn_d]}{2} \cdot V_{box} \right)_{t1} \quad (2)$$

where $Rn_d \left(\frac{dpm}{m^3} \right)$ (downstream station measurement) and $Rn_u \left(\frac{dpm}{m^3} \right)$ (upstream station measurement) are the measured Rn-222 activities for the lower and upper bounds of the box, respectively. $V_{box} (m^3)$ was the water volume within the box at the respective time steps, t1 and t2. The equation provides a robust estimate of the change in radon activity that has occurred over 30-minute intervals.

The water volume component within each box, $V_{box} (m^3)$ is estimated using a high resolution digital elevation model (DEM). Complete bathymetric coverage of the Duplin River was acquired with a multibeam echosounder (Viso, 2011), and the surrounding sub-aerial catchment elevation was measured with LiDAR flyovers (Hladick

et al., 2013). Bathymetric and land elevation data were integrated and gridded to construct a DEM of the Duplin River catchment (Hladick et al., 2013) (Figure 1). The DEM provided a unique basis for calculating water volumes as a function of tidal elevations throughout the Duplin watershed. Volume rating curves were established for individual sections of the Duplin River, where ArcGIS was used to calculate the flooded volume within each box as a function of water level measured at each time series station (Appendix A).

Radon inputs from downstream: $Rn_{ocean} \cdot Q_{in}$

We consider tidal intrusion during flood tide as a source of radon, as the incoming water has a defined radon activity. This is calculated as the radon activity in the ocean endmember multiplied by the tidal volume during each measurement interval. The term $Rn_{ocean} \left(\frac{dpm}{m^3} \right)$ is the estimated ocean activity entering the Duplin River from the Lower Duplin station (Figure 1). We took the lowest 25% of measurements from this station to represent the Rn_{ocean} term.

This term was applied to all sections as we assumed the majority of incoming water was of ocean origin. This term is multiplied by the respective $Q_{in} \left(\frac{m^3}{\Delta t} \right)$ to calculate the input of radon activity to each box from flood tide advection. Differences between two successive water volume measurements describe the net rate of water advection into a box (Q_{in}).

$$Q_{in} = (V_{box})_{t2} - (V_{box})_{t1} \quad (3)$$

Radon input from groundwater: $Rn_{gw} \cdot Q_{gw}$

Another source of radon to the Duplin River as shown in Equation 1 is from groundwater discharge. The $Rn_{gw} \left(\frac{dpm}{m^3} \right)$ term represents the Rn-222 activity in the groundwater endmember. The endmember values were assigned based upon the average radon activity of the sectioned sediment core samples from each site (Table 3). The groundwater discharge rate Q_{gw} is the unknown term that we are solving for.

Radon inputs from ^{226}Ra decay: $^{226}Ra \cdot \lambda_{Rn} \cdot V_{box}$

The time series radon stations measure the total radon activity within the river system. Radium (^{226}Ra) is continuous source of radon within the water column through parent isotope decay and needs to be accounted for.

Radium-226 measurements were collected by pumping 60 L of Duplin River water during flood tide through the MnO_2 acrylic fibers that adsorb radium isotopes from the water and concentrated them on the fibers (Moore and Reid, 1973). The MnO_2 acrylic fibers were then sealed for one week and counted on a RaDecc delayed coincidence counter for the ingrowth of Rn-222 based on Ra-226 decays (see methods in Peterson et al., 2009). The Rn-222 activity supported by Ra-226 decay is calculated by multiplying this dissolved Ra-226 activity by the decay constant of radon, $\lambda_{Rn} \left(\frac{1}{min} \right)$, and the volume of the box V_{box} .

Radon loss to upstream: $Rn_{out} \cdot Q_{out}$

One of the losses of radon from each box is due to tidal advection farther upstream. The $Rn_{out} \left(\frac{dpm}{m^3} \right)$ term consists of measured radon activity at the upstream measurement station multiplied by the total water discharge, $Q_{out} \left(\frac{m^3}{\Delta t} \right)$, which is calculated with equation (3) using the dimensions of the downstream box to obtain the water volume change within each box.

Radon losses to decay: $Rn_{box} \cdot \lambda_{Rn} \cdot V_{box}$

Radioactive decay of Rn-222 is calculated using the average radon activity $Rn_{box} \left(\frac{dpm}{m^3} \right)$ multiplied by the decay constant $\lambda_{222} (min^{-1})$ and volume of the box $V_{box} (m^3)$. The $Rn_{box} \left(\frac{dpm}{m^3} \right)$ term is averaged between the upper and lower boundary measurement stations at each time point.

$$Rn_{box} = \frac{[Rn_u] + [Rn_d]}{2} \quad (4)$$

Radon losses to the atmosphere: $A_{box} (J_{wind} + J_{current})$

The atmospheric evasion term consists of wind evasion, $J_{wind} \left(\frac{dpm}{m^2 hour} \right)$ and current evasion, $J_{current} \left(\frac{dpm}{m^2 hour} \right)$. The losses are dependent upon the Rn-222 concentration gradient across the air-water interface, temperature, wind velocity, and current velocity (Burnett and Dulaiova, 2003). Atmospheric evasion is a difficult parameter to estimate considering inherent spatial variability in both wind and current speed. We assumed a uniform wind field throughout the domain and current velocities

were estimated using time-step discharge rates in 30-minute intervals. $A_{box}(m^2)$ refers to the surface area of water inundation based on water level from the calibration curve set by the DEM. Both wind and current evasion used the equation:

$$J = k(Rn_{box} - aRn_{air}) \quad (5)$$

where $J \left(\frac{dpm}{m^2hour} \right)$ is the radon flux to the atmosphere, k is the piston velocity (gas transfer velocity; m/s), $Rn_{box} \left(\frac{dpm}{m^3} \right)$ is the Rn-222 activity within the water column, $Rn_{air} \left(\frac{dpm}{m^3} \right)$ is the activity in the air directly above the water column (assumed to be a constant 100 dpm m^{-3}), and a is the Ostwald solubility coefficient that describes the solubility of radon between aqueous and gaseous phases (cm hr^{-1}) (MacIntyre et al., 1995). The piston velocity that was driven by winds was calculated using:

$$k_{wind} = 0.45u^{1.6} \left(\frac{Sc}{600} \right)^{-a} \quad (6)$$

where u is wind speed in (m/s), Sc is the Schmidt number for radon at a given water temperature, and a is a variable power function that is dependent on wind speed. In addition to wind driven evasion, water current contribution to the atmospheric flux were estimated using the equation by (Borges et al., 2004) :

$$k_{current} = 1.719w^{0.5}D^{-0.5} \quad (7)$$

where $k_{current}$ is the piston velocity driven by current turbulence, w is the water current (cm/s) and D is the water depth (m).

Ebb tide conditions:

Changes in radon mass within each box during ebb tide (Figure 2B) result as a balance between inputs and outputs. However, due to directional movement of the water

during ebb tide, tidal influences represent somewhat different influences on the radon mass balance. The inputs consist of groundwater discharge, transport of river waters from adjacent boxes upstream, and ingrowth from dissolved Ra-226. For the uppermost section of the river, we did not consider transfer from farther upstream as a source of radon (the system terminates at this point). Outputs during ebb tide included tidal flushing of water fluxes downstream out of each box, radioactive decay, and atmospheric degassing. During ebb tide, the radon mass balance equation is:

$$\frac{\Delta Rn}{\Delta t} = \{([Rn_{in}] \cdot Q_{in}) + ([Rn_{gw}] \cdot Q_{gw}) + ([Ra_{226}] \cdot \lambda_{Rn} \cdot V_{box})\} - \{([Rn_{out}] \cdot Q_{out}) + ([Rn_{box}] \cdot \lambda_{222} \cdot V_{box}) + A_{box} \cdot (J_{wind} + J_{current})\} \quad (8)$$

in which the $Rn_{in} \left(\frac{dpm}{m^3}\right)$ term replaces $Rn_{ocean} \left(\frac{dpm}{m^3}\right)$ as the horizontal radon input to each box. All other terms in the ebb tide equation are the same as described in the flood tide equation. Equations (1) and (8) were solved for groundwater discharge, $Q_{gw} \left(\frac{m^3}{\Delta t}\right)$, for each 30 minute measurement interval.

2.3 Field Measurements: Electrical Resistivity:

Electrical resistivity data were collected using a stationary dipole-dipole time series approach where multiple measurements were collected over a tidal cycle. This approach results in a series of tomograms showing the change in subsurface electrical structure through time. The time-transient signal is a function of changes in porewater salinity. Electrical resistivity instrumentation consisted of a Supersting R8/IP internally logging resistivity meter with an 8-channel receiver, switch box, and custom-built 112 meter cable with 56 electrodes (2 meter spacing). The graphite electrodes were coupled to stainless steel spikes driven into the ground for increased surface contact. All

equipment is powered with a 12 volt deep-cycle marine battery and the source current is regulated by the Supersting unit where a maximum 2000 mA of electricity is injected into the ground.

Two sites were chosen for ER measurements to examine the river-marsh-upland interactions along the Duplin. Both ER transects were shore perpendicular and included sections of upland, marsh, and river bank. The Upper Duplin site extended across the upland (Figure 1A) into the adjacent salt marsh and terminated six meters into the intertidal mud flat of the Duplin River. The second site was located within the Central Duplin section, where a narrow marsh section is hydraulically connected to the island aquifer adjacent to the Central Duplin radon sampling site. The sites were chosen for accessibility and their geographic proximity to the radon time series stations. A total of four time series measurements were conducted at each site, two during spring tides, and two during neap tidal cycles. Multiple measurements were collected over 24-hr periods to capture the full range of porewater characteristics in relation each tidal cycle. During the ER measurement campaigns, water level and electrode inundation were recorded using a laser level to obtain transect terrain slope. Real-Time Kinematic (RTK) GPS was used to obtain accurate offsets for water level and land elevations to account for electrode inundation during post processing.

Measured resistivity values were processed into color-contoured tomograms using the inversion modeling software Earth Imager 2D, developed by Advanced Geosciences Inc (AGI). This model is designed to invert the field measurements of resistance (ohms) and construct a grid of spatial variability in subsurface resistivity (ohm-m). Multiple iterations varying geological scenarios converge upon a best-fit model between predicted

and measured resistivities. The iteration is complete when the statistical thresholds of L2-norm and root mean square error (RMS) between the model inversion and the actual measurements are within widely accepted minimal thresholds (RMS <10% and L2-norm < 1.0).

3. Results:

3.1 Field Measurements:

Radon time series measurements of the Duplin River were conducted from June 3th to June 27th 2013 (Figure 3). A 16-hour data gap between 6/6 and 6/7 resulted from mandatory evacuation of Sapelo Island due to Tropical Storm Andrea. Other data gaps from the Lower Duplin and Central Duplin stations resulted from data downloads and periodic maintenance. We observed a general trend of increasing radon activity from the Lower Duplin site near the mouth of the Duplin River towards the Upper Duplin site near the headwaters (Figure 4). On average, Upper Duplin radon activities were a factor of two greater than any other site (Figure 4 and 5). Radon activity varied inversely with water level across all three stations. A subsection of the Upper Duplin time series shows increased radon activity during ebb tides, and decreased radon activity during flood tide (Figure 6).

For most of the sampling period, salinity measurements varied directly with water level, suggesting a typical tidally-driven estuarine circulation pattern within the Duplin River (Figure 7). These measurements are consistent with the previously documented pattern of decreased salinity and dampened tidal amplitude towards the headwaters (McKay and Di Iorio 2010). In addition, the Upper Duplin section has a unique transition

where the typically covarying salinity and tidal records shifted completely out of phase during spring tide (Figure 7). A long term hydrological monitoring station near the Upper Duplin station confirmed an inverse estuary episode during large spring tides (<http://cdmo.baruch.sc.edu/>). The Central Duplin salinity records decreased in an uncharacteristic manner during the last week of sampling, likely due to sensor degradation.

Precipitation events were minimal and the noteworthy events occurred at the beginning and end of our month-long instrument deployment (Figure 3). At the beginning of our deployment, isolated thunderstorms (June 3rd through 7th) and tropical Storm Andrea (June 6th) resulted in a few brief episodes of rainfall and elevated wind speeds. Decreased radon activities were measured following the passage of Tropical Storm Andrea at all three sites (Figure 3). Afternoon precipitation due to thunderstorms did not result in decreased radon activity among the three sample sites. In general, during the days with afternoon showers, we observed increased radon activities in the Lower Duplin, steady levels in the Central Duplin, and slightly decreased radon activity in the Upper Duplin (Figure 3).

3.2 Groundwater Endmembers:

Given geological variability, sediment samples were analyzed for porewater Rn-222 endmember activity using the sediment equilibrium technique of Corbett et al. 1998 (Table 3). Our sediment equilibration averages at each site ranged 1.05×10^5 dpm m^{-3} for the Upper Duplin to 9.20×10^4 dpm m^{-3} in the Central and Lower Duplin river sections (Table 3).

In addition, grain size analysis was conducted down the length of each core in 10 cm intervals to classify sediment type along the Duplin River. The Upper Duplin exhibits a clear two-layer system with silty marsh sediments at the surface and an abrupt transition to medium to fine grained sands occurring at 40 cm depth in the high marsh core and 100 cm depth at the marsh channel. This transition indicates that the interface between the layers slopes towards the river channel. The Central Duplin and Lower Duplin cores contained a single-layer system consisting primarily of marsh silts. The Lower Duplin section also consisted of a shelly transitional layer at 200 cm depth grading into sand and silt below.

3.3 Groundwater Discharge Model:

The radon mass balance was constructed assuming radon inputs resulted from groundwater discharge within a given river segment, tidal currents from the adjacent segment, and decay from the parent isotope. Losses within a given segment included tidal discharge, radioactive decay, and atmospheric evasion (current + diffusion). The mass balance equation was solved for net groundwater discharge within each section (e.g., Upper, Central, Lower sections) of the river. In-situ radon time series measurements occurred at 30-minute intervals, and were summed over tidal cycles for site comparison (Figure 8 and 9).

The Upper Duplin section was characterized by a relatively constant groundwater discharge rate over the tidal cycle throughout the measurement period (Figure 8). The percentage of surface water comprised of recently discharged groundwater in the Upper Duplin section was greatest during neap tide (average: 6.9%) and significantly lower

during spring tide (average: 4.0%) (Figure 9). The Central Duplin displayed a similar trend of consistent groundwater discharge during the measurement period. While the Central Duplin section had a greater volume of groundwater discharge than the Upper Duplin section, the relative percentage of groundwater discharge was less because the total volume of the Central Duplin was greater (Figure 9). The Lower Duplin had the greatest volumetric groundwater discharge contribution to system, but in terms of percent composition, the Lower Duplin section contributed the least (Figure 9C). The Lower Duplin section was also characterized by an overall increase in groundwater discharge from neap to spring tides (Figure 9 and 10).

To standardize discharge rates, we integrated groundwater discharge over each tidal cycle in each section and normalized these results to the length of main channel shoreline (as $\text{m}^3 \text{m}^{-1} \text{cycle}^{-1}$) (Figure 10). There was a decreasing discharge trend from the upper reaches to the mouth, indicating a significant difference in groundwater discharge rate through the river. From neap to spring tide conditions, both the Upper and Central Duplin section showed a slight increase in discharge rate from $10.0 \text{ m}^3 \text{m}^{-1} \text{cycle}^{-1}$ to $11.8 \text{ m}^3 \text{m}^{-1} \text{cycle}^{-1}$ in the Upper Duplin section and $8.0 \text{ m}^3 \text{m}^{-1} \text{cycle}^{-1}$ to $8.1 \text{ m}^3 \text{m}^{-1} \text{cycle}^{-1}$ in the Central Duplin section. There was a substantially larger increase from $4.1 \text{ m}^3 \text{m}^{-1} \text{cycle}^{-1}$ to $6.3 \text{ m}^3 \text{m}^{-1} \text{cycle}^{-1}$ observed in the Lower Duplin section.

3.4 Electrical Resistivity:

Electrical resistivity measurements were conducted in the Upper and Central Duplin sections to image shallow marsh and upland aquifer processes (Figure 11 and 12). Multiple tomograms were collected along the same transect throughout a 24-hour period.

We were able to qualitatively characterize the shallow groundwater flow in the transition zone from the upland to the river channel where fresher and saltier porewaters were mixing. The resistivity varied along transects between 0.25 and 10 ohm-m, characteristic of shallow coastal sediments saturated with brackish to saline waters. Additional resistivity results are provided in Appendix C.

4. Discussion:

The four-week field deployment allowed for the characterization of variability in environmental conditions on Sapelo Island. During the first week of data collection, Tropical Storm Andrea made landfall near Sapelo Island. We conducted our field observations before and after the tropical storm that impacted the study site with a prolonged period of elevated wind and steady precipitation. Because radon is a gas and susceptible to atmospheric loss due to wind, we observed a decrease in radon activity within the water column across all three measurement stations immediately after the storm (Figure 3 and 6). During the last 10 days of the deployment several storm events yielded precipitation and wind totals similar to the tropical storm, but we did not observe similar decrease in radon activity resulting from these storms. This suggests an additional driver for radon variability other than precipitation and atmospheric evasion is affecting this system.

4.1 Radon Mass Balance:

Our non-steady state radon mass balance showed both positive and negative groundwater fluxes during a tidal cycle (Figure 8). Maximum groundwater discharge

coincided with greatest surface water discharges (Figure 13). This was expected, as groundwater discharge is a function of total discharge in our model resulting in variable groundwater discharge rates in the 30-minute time steps (Figure 8). The 30-minute groundwater discharge rates were integrated over complete tidal cycles (low tide - low tide) to provide a net value of groundwater input to the system. The model is a net balance (i.e., it accounts for both positive and negative groundwater discharge) suggesting the negative model values could be from unaccounted loss to the system.

Measured radon activities had an inverse relationship with water level, suggesting an increase in radon activity within a river section during ebb tide. This inverse relationship is typical of time series radon measurements in tidally pumped groundwater systems (Santos et al., 2011; Gleeson et al., 2013). During maximum ebb discharge from a river section, the loss of total radon due to volumetric change was still larger than the radon inputs, despite the elevated activity levels throughout the entire ebb tide. Therefore, the negative change in Rn-222 term (ΔRn) results in negative groundwater discharge estimates (Figure 8).

To test our non-steady state approach, we incorporated a steady state mass balance approach that assumes input terms equal loss terms:

$$\{([Rn_{in}] \cdot Q_{in}) + ([Rn_{gw}] \cdot Q_{gw}) + ([Ra_{226}] \cdot \lambda_{Rn} \cdot V_{box})\} = \{([Rn_{out}] \cdot Q_{out}) + ([Rn_{box}] \cdot \lambda_{222} \cdot V_{box}) + A_{box} \cdot (J_{wind} + J_{current})\} \quad (9)$$

When we arranged our variables in such a steady-state configuration, the majority of discharge values were positive throughout the tidal cycle in each section (Figure 14). Peak discharge still occurred during maximum volume change on both flood and ebb tides because of the dependency on water volume. In addition, the tidal cycle integrated

groundwater discharge totals for the non-steady state and steady state equations showed a strong 1:1 correlation (Figure 15).

To further examine our model behaviors, a sensitivity analysis was conducted by applying a +/-10% shift to each parameter:

{ $[Rn_{in}]$, $[Rn_{gw}]$, $[Ra_{226}]$, $[Rn_{out}]$, $[Rn_{box}]$, $(J_{wind} + J_{current})$ }. The adjusted values were input to the mass balance equation to calculate sensitivity of groundwater discharge results on each parameter (Table 1). Results of the sensitivity analysis indicated that three variables significantly control the variability in groundwater discharge: 1) tidal water flux into and out of a river section; 2) accounting for atmospheric loss; and 3) endmember radon concentration (Table 1). Endmember values and ebb tidal loss variables were significant across all three sites. Ebb tidal inputs and flood tidal outputs were significant in the Central and Lower Duplin segments. Atmospheric evasion had twice the impact in the Upper and Central Duplin sections than the Lower Duplin section, while flood tide inputs to the lower section were a factor of two and three greater than the Central and Upper Duplin sections, respectively.

Atmospheric evasion in general is more difficult to estimate because of the spatial and temporal variability in both wind speed and current velocity. Ebb dominated systems like the Duplin River have a greater ebb tide current velocity during spring tide (Ragotzkie and Bryson, 1955; Kjerfve, 1973; Zarillo, 1985). Our current velocity estimates were located at the sample stations, but bends and curves in the river system can alter current and mixing properties. We estimated currents based on water level measurements at the three time series sampling locations. Though these measurements provide a reasonable basis for determining atmospheric evasion, current velocities are

likely to be variable across and along the river channel. Many previous radon studies have not accounted for current evasion, but our study estimates 35% of the total atmospheric loss is driven by the surface water currents. Our estimation agrees with previous studies that show current evasion to be a substantial loss term and can have a significant effect on total groundwater discharge within a radon mass balance (Santos and Eyre, 2011; Makings et al., 2014).

Groundwater endmember values are often a major source of uncertainties and can vary on temporal and spatial scales (Burnett et al., 2007; Dulaiova et al., 2008). Radon endmembers derived from sediment equilibration experiments have been used in previous groundwater studies (Dulaiova et al., 2008). We accounted for endmember spatial variability along the river channel by taking sediment samples at multiple depths from two cores at each site. The near river and near upland sediment cores yielded similar radon activities, so average endmembers were assigned for each river section based on both cores (Table 3). The Upper Duplin section endmember activities were 14% greater than those calculated from the Central and Lower Duplin.

Normalizing groundwater discharge to main channel unit length provided a basis for spatial comparison between the river sections as well as temporal variations within the individual sections. Increases in side channel abundance upstream in the Duplin River increase marsh area in the headwaters. The total channel length was considered only for side channels greater than 15 meters wide. Channel widths of greater than 15 meters were distinctly visible via satellite imagery, this provided the basic shape of the Duplin River and excluded intertidal creeks of the associated salt marsh. The normalized

values indicate that total groundwater discharge decreased progressively downstream (Figure 10).

McKay (2008) estimated groundwater inputs to the Duplin River through an empirical salt balance model with the potential for groundwater inputs of $15 \text{ m}^3\text{s}^{-1}$. In contrast, our radon mass balance approach shows 30% less groundwater input to the Duplin River. This is a substantial difference considering a salt balance approach incorporates only fresh groundwater entering a system, while the radon mass balance approach integrates all sources regardless of composition. The differences in results are most likely linked to the measurement approaches as McKay (2008) stated the salt balance model estimate had limited in-situ salinity and water storage measurements. The salt balance model was only to be regarded as order of magnitude estimate. The radon mass balance approach had better constraints on water storage (DEM water fluxes) and incorporated groundwater tracers (Rn-222 measurement stations) to constrain the groundwater discharge to the Duplin River. Taking this into account, the radon mass balance approach is an improvement to groundwater discharge estimates in the Duplin River.

4.2 Electrical Resistivity:

The ER tomograms show clear evidence of tidal pumping in the shallow (<15 meters) aquifer (Figure 11 and 12). In the Upper Duplin section, seven measurement cycles throughout almost two complete tidal cycles show two layers of different resistivity (Figure 11). A lower resistivity layer extends to a depth of 6-7 meters, overlying a higher resistivity layer that connects to the freshwater lens beneath adjacent

upland. Both layers respond to tidal oscillations with substantial changes in resistivity within the proximity of the marsh and river channel. The shallow layer was consistently lower in resistivity with values approaching those expected for a formation saturated with salt water (< 1 ohm-m). During flood tide, surface water overtopped the marsh sediments and percolated into the muddy surficial aquifer. By high tide, resistivity values decreased, indicating complete saturation with the salty surface waters from the Duplin (Figure 11 D, E). At the same time, the deeper, higher resistivity layer was compressed landward, away from the river channel as lower resistivity (saltier) water infiltrated the aquifer. During the falling tide, the shallow layer showed evidence of discrete volumes of low resistivity water advecting through the aquifer matrix and discharging to the river channel while the deeper layer returned to discharging fresher water to the river channel (Figure 11 C-E).

The Upper Duplin station also showed vertical advection of higher resistivity waters during peak spring high tide (Figure 11 C, G). This unique observation suggests a tidally modulated connection between the shallow and deep layers, occurring only during the largest tidal amplitudes. This connection may occur due to the localized nature of the groundwater system associated with the marsh platform along the Upper Duplin. The upland (referred to as Moses Hammock) is decoupled from Sapelo Island and is fully surrounded by salty river water at high tide. As the salty, dense surface water infiltrates the perimeter of the hammock, the fresher, more buoyant water within the surficial hammock aquifer is squeezed and may be forced to advect vertically.

Variations among the tomograms from the Central Duplin site were not as dynamic throughout the measurement period (Figure 12). Overall, the aquifer remained

saltier with no clear evidence of a connection to the freshwater lens beneath Sapelo Island (not imaged in this study). This may be due to the location of the sampling transect on a cusp of Sapelo Island (Figure 1B). With the cusp largely surrounded by the waters of the Duplin River, saline water appears to remain in the aquifer throughout the tidal cycle. Similar to the Upper Duplin site, the resistivity of the marsh in the Central Duplin is controlled by the surface water inundation and percolation process. At approximately 40 meters along the transect line, a slightly higher resistivity (~2 ohm-m) layer is present consistently throughout the tidal cycle (Figure 11). Though the overall range of resistivity values are much narrower than the Upper Duplin site, this consistent layer is an indication of a horizontal transition from marsh sediments to upland sediments.

Saline intrusion (resistivity decrease) during flood tide and freshening (resistivity increase) during ebb tide supports the radon time series measurements as an indication that during tidal inundation hydraulic gradients favor saline intrusion into marsh sediments as recharge, whereas discharge from the marshes occurs during ebb tide. Tidal amplitude is also a significant control on shallow aquifer dynamics. The larger tidal range during spring tide results in more substantial saline water intrusion into the shallow aquifer system at both sites (Figure 16). During neap tide, at the Upper Duplin site, the deeper layer is far less compressed away from the river channel at high tide than during spring tide (Figure 16). At the Central Duplin site, the entire resistivity transect is far less variable throughout the fortnightly tidal cycle (Figure 16).

The Central Duplin transect showed a low resistivity region extending downward near the marsh-upland boundary (Figure 12, 34 meters along transect). This region swelled during rising flood tide and extended landward beneath the surficial

sediment layer. This feature was present during the two consecutive spring tides during June 2013. In addition to further documenting the influence of tidal pumping, this feature may indicate the influence of a “clogging layer” described by Schultz and Ruppel (2002). The clogging layer is envisioned as a boundary along the main island marsh, where the marsh mud material has infiltrated coarse upland sands, thus impeding groundwater flow and surface water interactions across the tidal creek boundary.

4.3 Groundwater dynamics:

Spring tides expose larger seepage areas and create greater hydraulic gradients (Wilson and Gardner, 2006; Wilson and Morris, 2012). This can result in enhanced tidal pumping and greater net groundwater discharge from the island aquifer. The electrical resistivity time series tomograms showed a change in subsurface electrical properties correlating with the tidal amplitude (Figure 16). The tomograms showed spring tide conditions imposed a greater effect on the subsurface exchange suggesting that tidal pumping is a primary driver of groundwater exchange in the Duplin River system. However, the groundwater discharge model results do not show a significant difference in groundwater discharge between spring and neap tides, likely due to the complex nature a back barrier system (Figure 10). This suggests the system has a complex hydrogeologic matrix that contributes to groundwater discharge to the Duplin River.

The combined effect of tidal amplitude and river channel-marsh geomorphology can be a significant factor in exchange of groundwater. The three river sections had significant differences in inundation area between spring and neap conditions, with the Upper Duplin river section containing the largest difference in inundation area (Table 2).

The majority of seepage occurs within several meters of the intertidal creek bank (Gardner, 2005). It has been proposed that the dynamics of seepage alone could provide most if not all of the oxygen and sulfate need for decomposing below ground *Spartina* biomass, as well as volumetric flushing of the sulfide and demineralized nitrogen and phosphorus (Gardner, 2005). The Upper Duplin has many side channels that add to seepage face surface area, and thus the total headwater seepage area may allow for greater horizontal and vertical infiltration into the marsh sediments. This leads to a larger mixing zone and helps explain the significantly greater groundwater input in the Upper Duplin section. As tidally-driven seepage leads to flushing and cycling of chemicals constituents and enhanced creek side productivity within the salt marsh system (Gardner, 2007; Schutte et al., 2013), the headwaters of the Duplin may be critical in driving the vast surrounding marsh ecosystem.

A major groundwater source is likely to occur where aquifers have been incised by the main river channel. Continuous under-way (boat-based) radon measurements of the Duplin River have indicated increased radon activities towards the headwaters and several specific zones that were in close proximity to deep scours observed in the high-resolution multibeam bathymetry (Peterson, unpublished data). These scour sites have likely exposed coarser aquifer sediment for greater discharge potential. In addition, greater current velocities creating the scours likely keep finer materials from potentially settling and clogging pore spaces. Though aquifers are no longer artesian due to anthropogenic pumping of the greater Floridian aquifer, direct freshwater input at known aquifer-river channel intersections is likely an additional source (Kjerfve, 1973; Alkaff,

2001). This may contribute to calculated groundwater discharge during flood tide in our discharge model.

In addition, the exposed sites may discharge radon-enriched water through cross island tidal pumping. A study in the Florida Keys has shown a connection between Atlantic tidal fluctuations and its influence on groundwater seepage in a back barrier setting (Chanton et al., 2003). Radon modeling efforts showed an inversely correlated peak with the Atlantic tide, suggesting that pressure head variations may drive groundwater seepage in a system.

The influence of freshwater entering the Duplin River via the Altamaha River can dilute the salinity in the Lower and Central regions of the Duplin. Recent transport models of the Altamaha River (Di Iorio and Castelao 2013) show the complex connections of the back barrier salt marsh systems can play a crucial role in transporting freshwater into Dobby Sound and potentially influence the Duplin River. If the incoming Altamaha River water is radon rich, we would expect to see increased radon activity during flood tides. However, the current mass balance equation should account for incoming horizontal radon inputs during flood tide. Further investigation is needed to constrain the effect of Altamaha River discharge has on our groundwater estimates. The influence of the Altamaha River may have a greater effect when incorporating a salt balance model to estimate groundwater discharge in the Duplin River. These processes could explain why the salt balance model (Mckay 2008) groundwater discharge estimates were greater than our current estimates.

Groundwater exchange has been estimated at geologically similar locations such as the North Inlet in South Carolina with groundwater discharge estimates of 10-40 L m⁻²

d^{-1} (Whiting and Childers, 1989; Morris, 1995; Krest et al., 2000). Discharge estimates for the Duplin River were substantially higher with values averaging $67 \text{ L m}^{-2} \text{ d}^{-1}$, almost double those at North Inlet. Santos et al. (2010) showed peaks in groundwater discharge rates of $16\text{-}62 \text{ cm day}^{-1}$ at the upper most points in Indian River Lagoon estuary. These values are similar to observed rates in the Duplin River estuary, where maximum discharge is measured near the headwaters and minimum discharge is measured near the mouth of the river. Differences in groundwater discharge are most likely due to tidal amplitude variation, greater seepage, and geological and hydrologic dynamics of a back barrier tidal marsh compared to an estuary that has a direct inlet to the open ocean.

5. Conclusions:

The combination of electrical resistivity and the geochemical tracer Rn-222 provides an excellent basis to describe and quantify groundwater in the coastal zone. The observational data can be used to constrain aquifer characteristics used in numerical simulations of chemical and nutrient transport within systems of similar structure. Our non-steady state radon mass balance, constrained by a continuous digital elevation model, provided a high-resolution quantitative determination of tidally-driven groundwater inputs to the Duplin River. Details of both temporal (semidiurnal and fortnightly) variation and spatial patterns of groundwater along the Duplin river channel are revealed by our observations. Daily patterns are observed in the radon activity throughout the Duplin River with the highest activities located near the headwaters, and gradually decreased towards the mouth. These observations are supported by our calculations that show groundwater discharge is greatest near the headwaters, where the marsh system has

an extensive network of side creeks. The fortnightly scales suggest tidal influences have a substantial influence on the groundwater dynamics. These conclusions are further constrained with the electrical resistivity tomograms. The time series images show saline intrusion during flood tide and porewater freshening during ebb that correlates with the radon measurements. The resistivity images show a distinct difference in the subsurface resistivity between spring and neap tide conditions.

Recommendations for future work include placement of a well transect coupled with a resistivity measurements to benefit resistivity model interpretations for possible horizontal groundwater transport rates. A resistivity transect (less than 1 m spacing) that extends to the center of the river channel would provide a higher resolution model. Time series radon measurements conducted in multiple seasons would provide improved temporal groundwater discharge variability. The use of the Duplin River DEM to evaluate scour marks as potential groundwater discharges points may highlight point source discharge. An incorporation of a salt-balance model with our radon mass balance equation would further constrain the groundwater dynamics of the Duplin River.

The data collected has provided baseline groundwater contributions to the Duplin River system. Adaptations to the radon mass balance such as incorporating a residency time term for water parcels that are not flushed in successive tides. Better constraints on the box volumes and water level data will significantly increase the model confidence, as the premises of the equation is linked to the discharge (Q) of surface water to compute our groundwater portion.

LITERATURE CITED

- Alkaff, H.F., 2001. Effects of regional anthropogenic groundwater alterations on groundwater levels of the Sapelo Island complex, Georgia. Proceedings of the 2001 Georgia Water Resources Conference. 760-763.
- Blanton, J., Andrade, F., Adelaide Ferreira, M., Amft, J., 2007. A digital elevation model of the Duplin River intertidal area. University of Georgia, Athens.
- Borges, A., Delille, B., Schiettecatte, L.S., Gazeau, F., Abril, G., Frankignoulle, M., 2004. Gas transfer velocities of CO₂ in three European estuaries (Randers Fjord, Scheldt and Thames). *Limnology and Oceanography* 49, 1630-1641.
- Burger, R.H., Sheehan, A.F., Jones, C.H., 2006. Introduction to applied geophysics. W.W. Norton & Company New York, London. ISBN-13: 978-0-393-92637-8
- Burnett, W.C., Dulaiova, H., 2003. Estimating the dynamics of groundwater input into the coastal zone via continuous radon-222 measurements. *Journal of Environmental Radioactivity* 69, 21-35. doi:10.1016/S0265-931X(03)00084-5
- Burnett, W.C., Kim, G., Lane-Smith, D., 2001. A continuous radon monitor for assessment of radon in coastal ocean waters. *Journal of Radioanalytical and Nuclear Chemistry* 249, 167-172.

Burnett, W.C., Aggarwal, P.K., Aureli, A., Bokuniewicz, H., Cable, J.E., Charette, M.A., Kontar, E., Krupa, S., Kulkarni, K.M., Loveless, A., Moore, W.S., Oberdorfer, J.A., Oliveira, J., Ozyurt, N., Povinec, P., Privitera, A.M.G., Rajar, R., Ramessur, R.T., Scholten, J., Stieglitz, T., Taniguchi, M., Turner, J.V., 2006a. Quantifying submarine groundwater discharge in the coastal zone via multiple methods. *Science of the Total Environment* 367, 498-543.
doi:10.1016/j.scitotenv.2006.05.009

Burnett, W.C., Santos, I.R., Weinstein, Y., Swarzenski, P.W., Herut, B., 2007. Remaining uncertainties in the use of Rn-222 as a quantitative tracer of submarine groundwater discharge. In: W. Sanford, C. Langevin, M. Pormio and P. Povinec (Eds), *A New focus on groundwater-seawater interactions*. IAHS Publ. 312, Perugia, Italy, pp. 109-118.

Chanton, J.P., Burnett, W.C., Dulaiova, H., Corbett, R., Taniguchi, M., 2003. Seepage rate variability in Florida Bay driven by Atlantic tidal height. *Biogeochemistry* 66, 187-202.

Charette, M.A., Scholten, J.G., 2008. The Renaissance of Radium Isotopic Tracers in Marine Processes Studies. *Marine Chemistry* 109, 185-187.

Corbett, D.R., Burnett, W.C., Cable, P.H., Clark, S.B., 1998. A multiple approach to the determination of radon fluxes from sediments. *Journal of Radioanalytical and Nuclear Chemistry* 7, 247-253. doi:10.1007/BF02386351

Daily, W., Ramirez, A., Binley, A., LeBrecque, D., 2004. Electrical resistance tomography. *The Leading Edge* 23, 438-442. doi: 10.1190/1.1729225

Di Iorio, D., Castelao, R., 2013. The Dynamical Response of Salinity to Freshwater Discharge and Wind Forcing in Adjacent Estuaries on the Georgia Coast. *Oceanography* 26, 44–51. doi:10.5670/oceanog.2013.44

Dulaiova, H., Gonnee, M.E., Henderson, P.B., Charette, M.A., 2008. Geochemical and physical sources of radon variation in a subterranean estuary — Implications for groundwater radon activities in submarine groundwater discharge studies. *Marine Chemistry* 110, 120–127. doi:10.1016/j.marchem.2008.02.011

Frey, R.W., Basan, P., 1985. Coastal salt marshes. In: Davis, R.A., Jr., (Ed), *Coastal Sedimentary Environments*, 2nd Ed. Springer-Verlag, New York.

Gardner, L.R., 2005. Role of geomorphic and hydraulic parameters in governing pore water seepage from salt marsh sediments. *Water Resource Research* 41, W07010. doi:10.1029/2004WR003671

- Gardner, L.R., 2007. Role of stratigraphy in governing pore water seepage from salt marsh sediments. *Water Resource Research* 43, W07502.
doi:10.1029/2006WR005338
- Gleeson, J., Santos, I.R., Maher, D.T., Golsby-Smith, L., 2013. Groundwater–surface water exchange in a mangrove tidal creek: Evidence from natural geochemical tracers and implications for nutrient budgets. *Marine Chemistry* 156, 27-37.
doi:10.1016/j.marchem.2013.02.001
- Hladik, C., Schalles, J., Alber, M., 2013. Salt marsh elevation and habitat mapping using hyperspectral and LIDAR data. *Remote Sensing of Environment* 139, 318 -330.
doi:10.1016/j.rse.2013.08.003
- Hoyt, J.H., 1967. Barrier island formation. *Geological Society of America Bulletin* 78, 1125-1136.
- Johnson, A.F., Barbour, M.G., 1990. Dunes and maritime forests. In R.L. Myers and JJ Ewel, editors. *Ecosystems of Florida*. University Press of Florida, Gainesville, pp. 429-480
- Johannes R.E., 1980. The ecological significance of the submarine discharge of groundwater. *Marine Ecology Progress Series* 3, 365-373.

- Kim, J.-S., Lee, M.J., Kim, J., Kim, G., 2010. Measurement of temporal and horizontal variations in ^{222}Rn activity in estuarine waters for tracing groundwater inputs. *Ocean Science Journal* 45, 197-202. doi:10.1007/s12601-010-0018-z
- Kjerfve, B., 1973. Volume transport, salinity distribution and net circulation in the Duplin Estuary, Georgia. Master's Thesis Marine Institute, University of Georgia.
- Krest, J., Moore, W.S., Gardner, R.L., Morris, T.J., 2000. Marsh nutrient export supplied by groundwater discharge: evidence from radium measurements. *Global Biogeochemical Cycles* 14, 167-176.
- Lanesky, D.E., Logan, B.W., Brown, R.G., Hine, A.C., 1979. A new approach to portable vibracoring underwater and on land: Method Paper. *Journal of Sedimentary Petrology* 49, 654-657.
- Macintyre, S., Wanninkhof, R., Chanton, J.P., 1995. Trace gas exchange across the air-sea interface in freshwater and coastal marine environments. In: Matson, P.A., Harris, R.C. (eds.), *Biogenic Trace Gases: Measuring Emissions from Soil and Water*. Blackwell Science Ltd, pp. 52-97.
- Makings, U., Santos, I.R., Maher, D.T., Golsby-Smith, L., Eyre, B.D., 2014. Importance of budgets for estimating the input of groundwater-derived nutrients to an

eutrophic tidal river and estuary. *Estuarine, Coastal and Shelf Science* 143, 65-76.
doi:10.1016/j.ecss.2014.02.003

Manheim, F.T., Krantz, D.E., Bratton, J.F., 2004. Studying ground water under Delmarva Coastal Bays using electrical resistivity. *Ground Water* 42, 1052-1068.

McKay, P., 2008. Temporal and spatial variability of transport and mixing mechanisms using heat and salt in the Duplin River, Georgia. Ph.D. Dissertation, University of Georgia, Athens, GA.

McKay, P., Di Iorio, D., 2010. Cycle of vertical and horizontal mixing in a shallow tidal creek. *Journal of Geophysical Research* 115, C01004. doi:10.1029/2008JC005204

Moore, W.S., Reid, D.F., 1973. Extraction of radium from natural waters using manganese-impregnated acrylic fibers. *Journal of Geophysical Research* 78, 8880-8886. doi:10.1029/JC078i036p08880

Moore, W.S., 1999. The subterranean estuary: a reaction zone of ground water and sea water. *Marine Chemistry* 65, 111-125. doi:10.1016/S0304-4203(99)00014-6

Morris, J.T., 1995. The mass balance of salt and water in intertidal sediments: Results from North Inlet, South Carolina. *Estuaries* 18, 556-567. doi:10.2307/1352376

- Nakada, S., Yasumoto, J., Taniguchi, M., Ishitobi, T., 2011. Submarine groundwater discharge and seawater circulation in a subterranean estuary beneath a tidal flat. *Hydrological Processes* 25, 2755-2763.
- Peterson, R.N., Burnett, W.C., Dimova, N., Santos, I.R., 2009. Comparison of measurement methods for radium-226 on manganese-fiber. *Limnology and Oceanography Methods* 7, 196–205. doi:10.4319/lom.2009.7.196
- Peterson, R.N., Santos, I.R., Burnett, W.C., 2010. Evaluating groundwater discharge to tidal rivers based on a Rn-222 time series approach. *Estuarine, Coastal and Shelf Science* 86, 165-178. doi:10.1016/j.ecss.2009.10.022
- Ragotzkie, R., Bryson R., 1955. Hydrography of the Duplin River, Sapelo Island, Georgia, *Bulletin of Marine Science of the Gulf and Caribbean*. 5, 297-314.
- Santos, I.R., Burnett, W.C., Chanton, J., Mwashote, B., Suryaputra, I.G.N.A., Dittmar, T., 2008. Nutrient biogeochemistry in a Gulf of Mexico subterranean estuary and groundwater-derived fluxes to the coastal ocean. *Limnology and Oceanography* 53, 705-718. doi:10.4319/lo.2008.53.2.0705
- Santos, I.R., Peterson, R.N., Eyre, B.D., Burnett, W.C., 2010. Significant lateral inputs of fresh groundwater into a stratified tropical estuary: Evidence from radon and

radium isotopes. *Marine Chemistry* 121, 37-48.

doi:10.1016/j.marchem.2010.03.003

Santos, I.R., Eyre, B.D., 2011. Radon tracing of groundwater discharge into an Australian estuary surrounded by coastal acid sulfate soils. *Journal of Hydrology* 396, 246-257. doi:10.1016/j.jhydrol.2010.11.013

Santos, I.R., Eyre, B.D., Huettel, M., 2012. The driving forces of pore water and groundwater flow in permeable coastal sediments: A review. *Estuarine, Coastal and Shelf Science* 98, 1-15. doi:10.1016/j.ecss.2011.10.024

Schultz, G., Ruppel, C., 2002. Constraints on hydraulic parameters and implications for groundwater flux across the upland–estuary interface. *Journal of Hydrology* 260, 255–269. doi:10.1016/S0022-1694(01)00616-3

Schultz, G.M., Ruppel, C., Fulton, P., 2007. Integrating hydrologic and geophysical data to constrain coastal surficial aquifer processes at multiple spatial and temporal scales, In: Hyndman, D.W., Day-Lewis, F.D., Singha, K. (Eds.). *Geophysical Monograph Series*. American Geophysical Union, Washington, D. C., pp. 161-182.

Schutte, C.A., Hunter, K., McKay, P., Di Iorio, D., Joye, S.B., Meile, C., 2013. Patterns and controls of nutrient concentrations in a southeastern United States tidal creek. *Oceanography* 26, 132-139.

Slomp, C.P., Van Cappellen, P., 2004. Nutrient inputs to the coastal ocean through submarine groundwater discharge: controls and potential impact. *Journal of Hydrology* 295, 64-86. doi:10.1016/j.jhydrol.2004.02.018

Swarzenski, P.W., Burnett, W.C., Greenwood, W.J., Herut, B., Peterson, R., Dimova, N., Shalem, Y., Yechieli, Y., Weinstein, Y., 2006. Combined time series resistivity and geochemical tracer techniques to examine submarine groundwater discharge at Dor Beach, Israel. *Geophysical Research Letters* 33, L24405. doi:10.1029/2006GL028282

Swarzenski, P.W., Reich, C., Kroeger, K.D., Baskaran, M., 2007a. Ra and Rn isotopes as natural tracers of submarine groundwater discharge in Tampa Bay, Florida. *Marine Chemistry* 104, 69-84. doi:10.1016/j.marchem.2006.08.001

Swarzenski, P.W., Simonds, F.W., Paulson, A.J., Kruse, S., Reich, C., 2007b. Geochemical and geophysical examination of submarine groundwater discharge and associated nutrient loading estimates into Lynch Cove, Hood Canal, WA. *Environmental Science & Technology* 41, 7022-7029.

- Tait, D.R., Santos, I.R., Erler, D.V., Befus, K.M., Bayani Cardenas, M., 2013. Estimating submarine groundwater discharge in a South Pacific coral reef lagoon using different radioisotope and geophysical approaches. *Marine Chemistry* 156, 49-60.
- Taniguchi, M., Burnett, W.C., Cable, J.E., Turner, J.V., 2002. Investigation of submarine groundwater discharge. *Hydrological Processes* 16, 2115-2129.
- Taniguchi, M., Burnett, W.C., Smith, C.F., Paulsen, R.J., O'Rourke, D., Drupa, S.L., Christoff, J.L., 2003. Spatial and temporal distributions of submarine groundwater discharge rates obtained from various types of seepage meters at a site in Northeastern Gulf of Mexico. *Biogeochemistry* 66, 35-53.
- Thompson, L.D.P., Miller, C.S., Doss, P.K., Baedke, S.J., 1991. Land-based vibracoring and vibracore analysis: tips, tricks, and traps. Department of Natural Resources, Geological Survey.
- Wadsworth, J.R., 1980. Geomorphic characteristics of tidal drainage networks in the Duplin River System, Sapelo Island, Georgia. Ph.D. Dissertation, University of Georgia, Athens, GA.
- Whiting, G.J., Childers, D.L., 1989. Subtidal advective water flux as a potentially important nutrient input to southeastern U.S.A. Saltmarsh estuaries. *Estuarine, Coastal and Shelf Science* 28, 417-431. doi:10.1016/0272-7714(89)90089-9

- Wilson, A.M., Gardner, L.R., 2006. Tidally driven groundwater flow and solute exchange in a marsh: Numerical simulations. *Water Resource Research* 42, W01405. doi:10.1029/2005WR004302
- Wilson, A.M., Morris, J.T., 2012. The influence of tidal forcing on groundwater flow and nutrient exchange in a salt marsh-dominated estuary. *Biogeochemistry* 108, 27-38. doi:10.1007/s10533-010-9570-y
- Valiela, I., Costa, J., Foreman, K., Teal, J.M., Howes, B., Aubrey., 1978. Transport of groundwater-born nutrients from watersheds and their effects on coastal waters. *Biogeochemistry* 10, 177-197.
- Viso, R.F., 2011. Digital Elevation Model (DEM) of the Duplin River and adjacent intertidal areas near Sapelo Island, Georgia. Georgia Coastal Ecosystems LTER Project; University of Georgia; Long Term Ecological Research Network.
- Zarillo, G.A., 1982. Stability of bedforms in a tidal environment. *Marine Geology* 48, 337–351. doi:10.1016/0025-3227(82)90103-7
- Zarillo, G.A., 1985. Tidal dynamics and substrate response in a salt-marsh estuary. *Marine Geology* 67, 13–35. doi:10.1016/0025-3227(85)90146-X

Zhang, J., Mandal, A.K., 2012. Linkages between submarine groundwater systems and the environment. *Current Opinion in Environmental Sustainability, Carbon and nitrogen cycles* 4, 219-226. doi:10.1016/j.cosust.2012.03.006

Zhou, W., Beck, B.F., Stephenson, J.B., 2000. Reliability of dipole-dipole electrical resistivity tomography for defining depth to bedrock in covered karst terrains. *Environmental Geology* 39, 760-766.

TABLES

Table 1: Results of the marsh sediment equilibration measurements arranged by depth profiles. Radon-222 measurement errors represent 1- σ uncertainties.

Location	Core Depth (cm)	Percent Water	Rn-222 (dpm m⁻¹)
Upper Duplin Near upland (N31 28.66' W81 16.34')	15	43	19,000 \pm 1,900
	35	45	63,000 \pm 4,000
	55	22	21,000 \pm 1500
	85	20	17,000 \pm 19,000
	155	20	272,000 \pm 13,000
	205	22	141,000 \pm 23,000
Upper Duplin Near River (N31 28.662' W81 16.351')	25	69	49,000 \pm 19,000
	75	61	84,000 \pm 19,000
	115	23	233,000 \pm 13,000
	175	20	153,000 \pm 8,000
Central Duplin Near Upland (N31 27.49' W81 16.69')	25	65	-
	75	62	85,000 \pm 4,000
	115	63	99,000 \pm 5,000
	165	56	82,000 \pm 24,000
Central Duplin Near River (N31 27.493' W81 16.695')	25	61	130,000 \pm 23,000
	75	62	115,000 \pm 34,000
	135	61	90,000 \pm 5,000
	185	53	46,000 \pm 30,000
Lower Duplin Near upland (N31 25.028' W81 17.70')	25	54	95,000 \pm 23,000
	55	51	104,000 \pm 5,000
	85	55	95,000 \pm 5,000
	125	61	85,000 \pm 20,000
	185	58	98,000 \pm 6,000
	215	24	85,000 \pm 16,000
Lower Duplin Near River (N31 25.05' W81 17.744')	25	46	108,000 \pm 6,000
	55	48	116,000 \pm 8,000
	85	56	84,000 \pm 4,000
	145	60	67,000 \pm 17,000
	205	59	84,000 \pm 33,000

Table 2: Summary of the sensitivity analysis of individual parameter influence on groundwater discharge values. Individual parameters were altered 10% and input into the radon mass balance equation for analysis. * indicates a parameter has a significant role in the groundwater discharge value.

Parameter	Upper Duplin (%)	Central Duplin (%)	Lower Duplin (%)
Inventory	0.16	0.18	1.00
Ra-226	0.02	0.05	0.13
Rn-222 Decay	0.54	1.23	1.78
Jatm	4.23*	4.50*	2.71
Flood in	1.94	3.11	6.57*
Flood Out	-	7.20*	9.36*
Ebb In	-	7.20*	8.68*
Ebb Out	7.49*	7.50*	12.44*
Endmember	10*	10*	10*

Table 3: Surface area coverage of spring and neap conditions for the various Duplin River sections. Surface areas shown are the average tidal amplitude during the spring and neap conditions. The percent change reflects the increase in section surface area compared during spring tide compared to neap tide.

Site	Spring Tide (m²)	Neap Tide (m²)	Percent Change %
Upper Duplin	9.75E+05	5.89E+05	65.51
Central Duplin	1.50E+06	1.14E+06	31.25
Lower Duplin	3.12E+06	2.08E+06	50.18

FIGURES

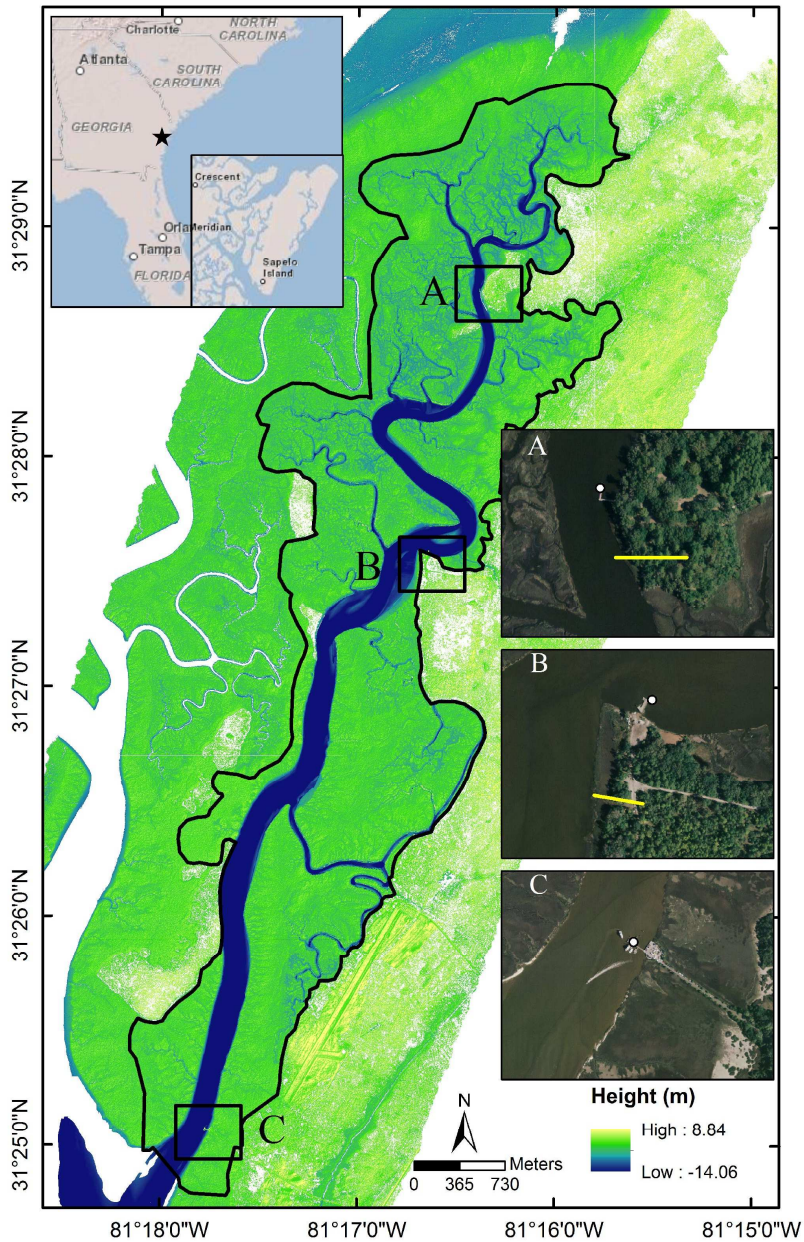


Figure 1: Location of the study site on Sapelo Island, Georgia. The main panel is a digital elevation model of the Duplin River catchment (outline in Black). Inserts show time series radon stations (white circles) and resistivity transects (yellow lines) at Upper Duplin (A), Central Duplin (B), and Lower Duplin (C) stations.

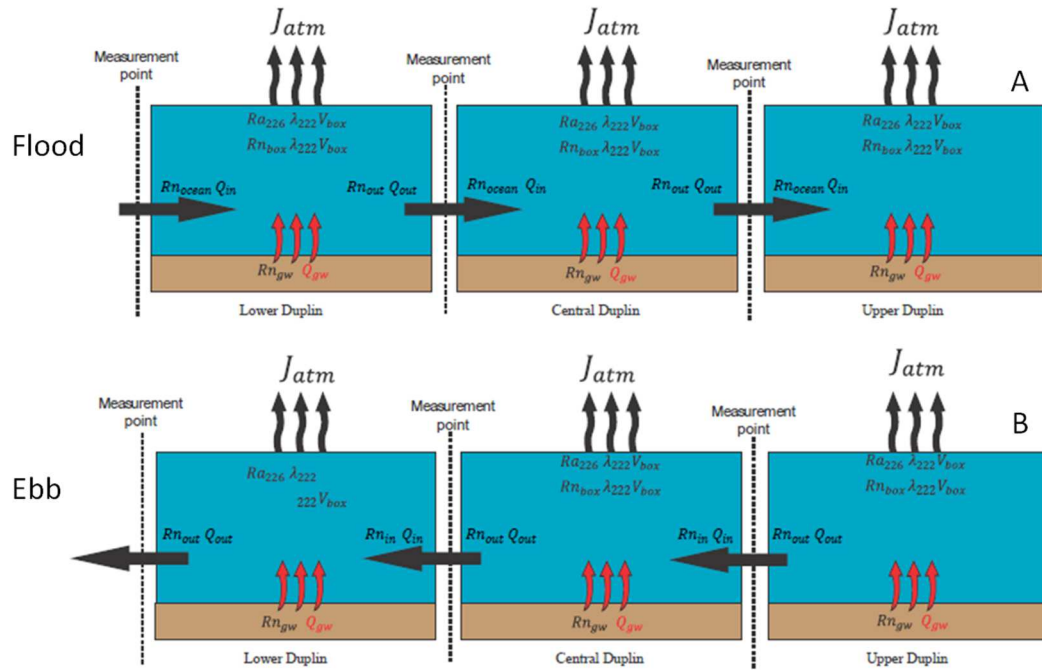


Figure 2: Conceptual model of our 3-box radon mass balance model. The dashed line between the boxes indicates the position of our radon time series stations and defines the dimensions of each river section. The arrows represent the flow of water (and therefore radon) into and out of each box during flood tide (A) and ebb tide (B).

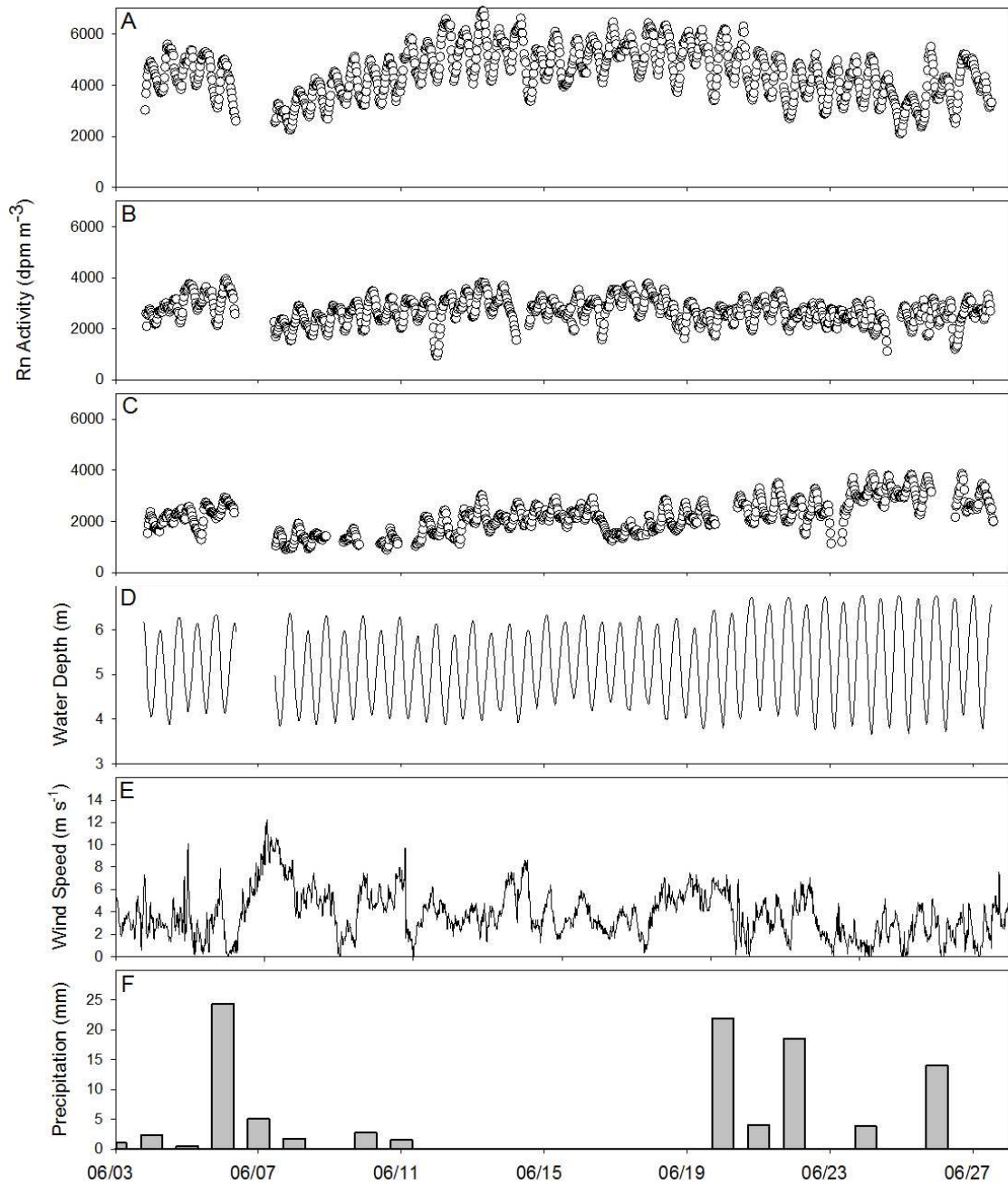


Figure 3: Time series graphs of the field parameters collected during the study. Surface water radon activity for Upper Duplin (A), Central Duplin (B), Lower Duplin (C), water levels from Upper Duplin (representative of tidal characteristics; D), wind speeds (E) and precipitation (F) are shown for our June 2013 observations.

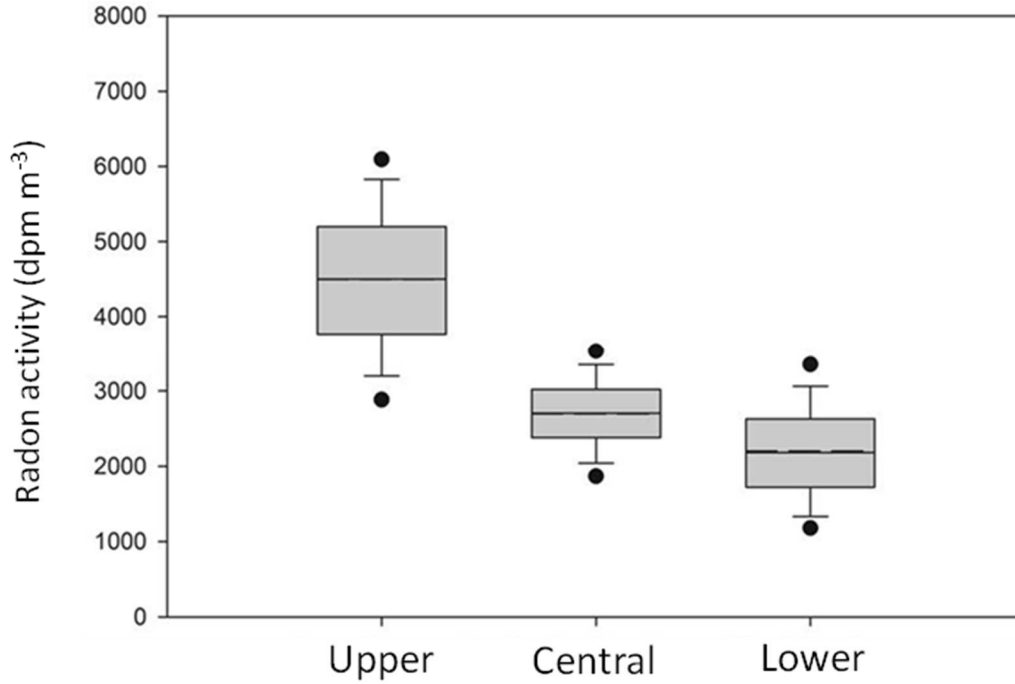


Figure 4: Observed radon activities from the three measurement stations (30 minute interval measurements). Box plots show median values (solid horizontal line), mean (dashed line), 50th percentile values (box outline), 10th and 90th percentile values (whiskers), and 5th/95th outlier values (black circles).

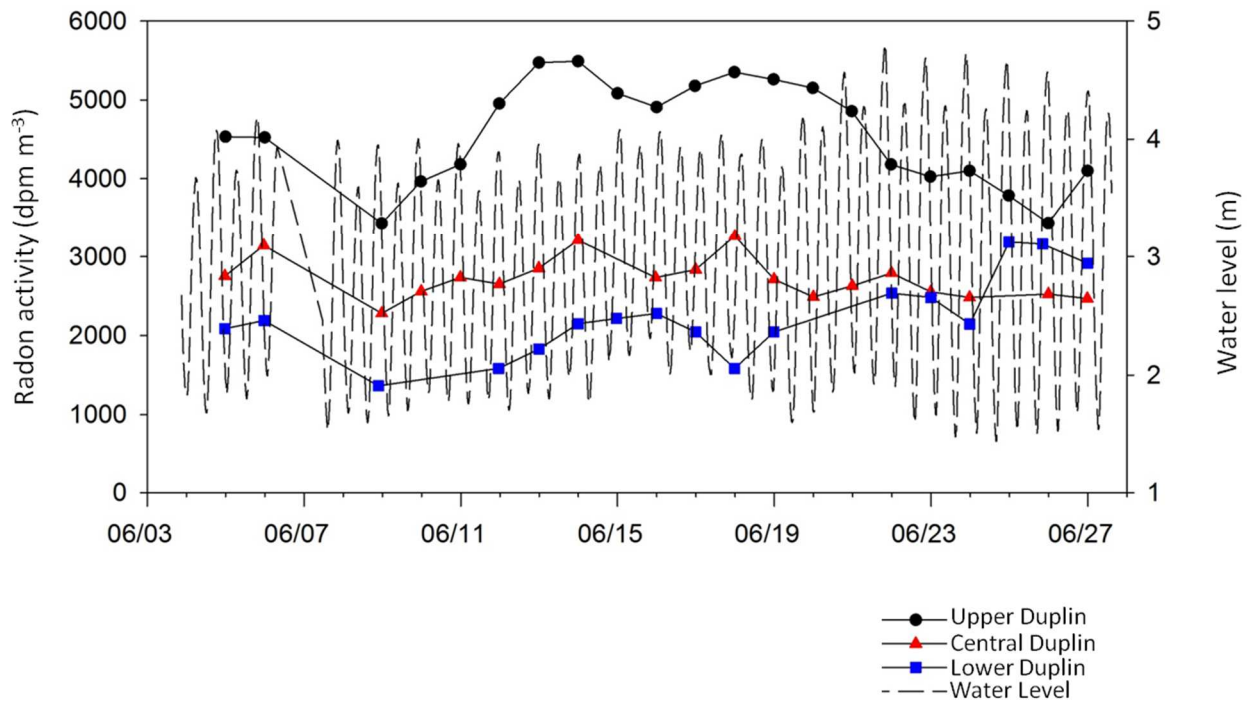


Figure 5: Average daily radon activities during the deployment in relation to the tidal trends of the Duplin River.

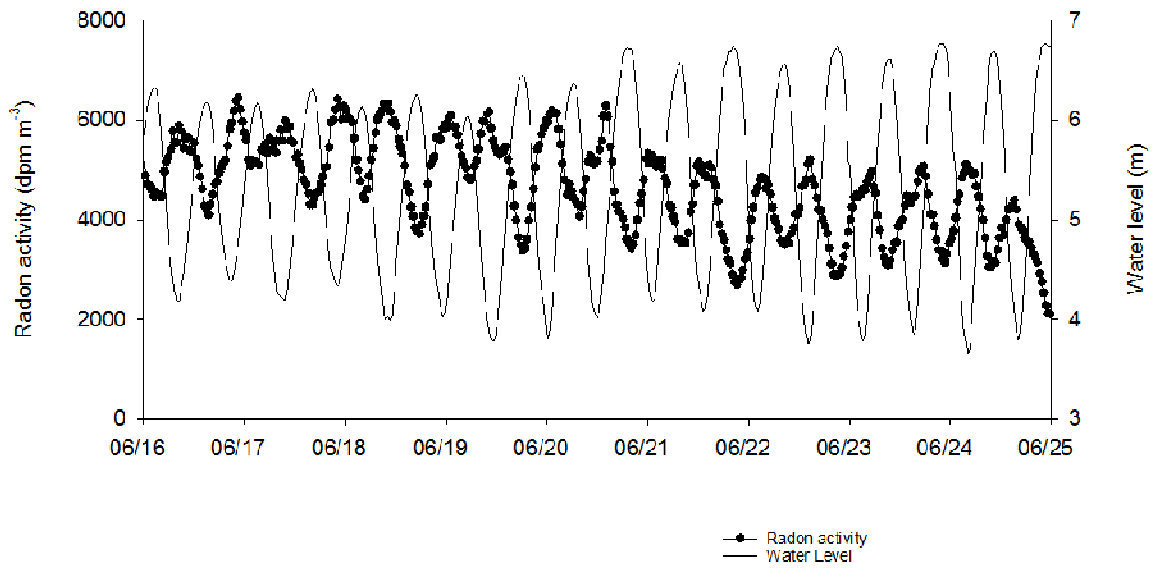


Figure 6: Radon activities at the Upper Duplin site shows an inverse correlation with water level. High radon activities occur during low water levels, and low radon activity during high water levels.

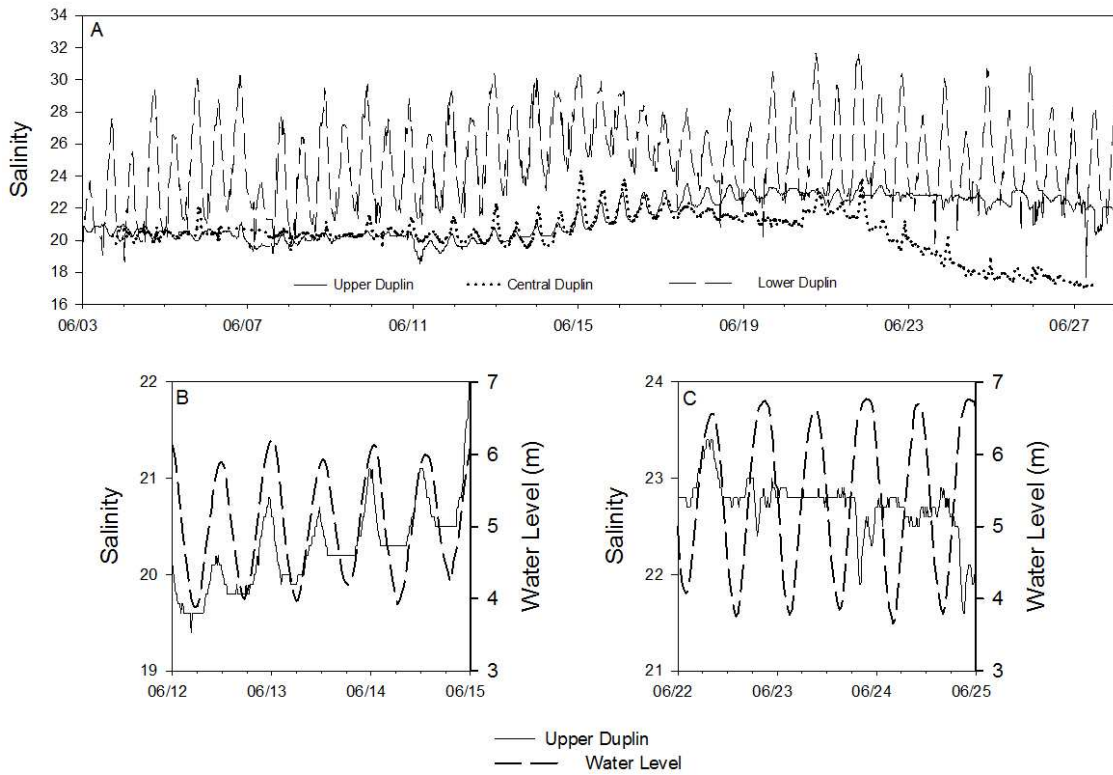


Figure 7: Time series salinity measurements from Upper Duplin, Central Duplin, and Lower Duplin (A). Salinity and water level are compared from the Upper Duplin station under neap (B) and spring (C) tidal conditions. Note the salinity reversal on 6/23 that occurs only at Upper Duplin (C).

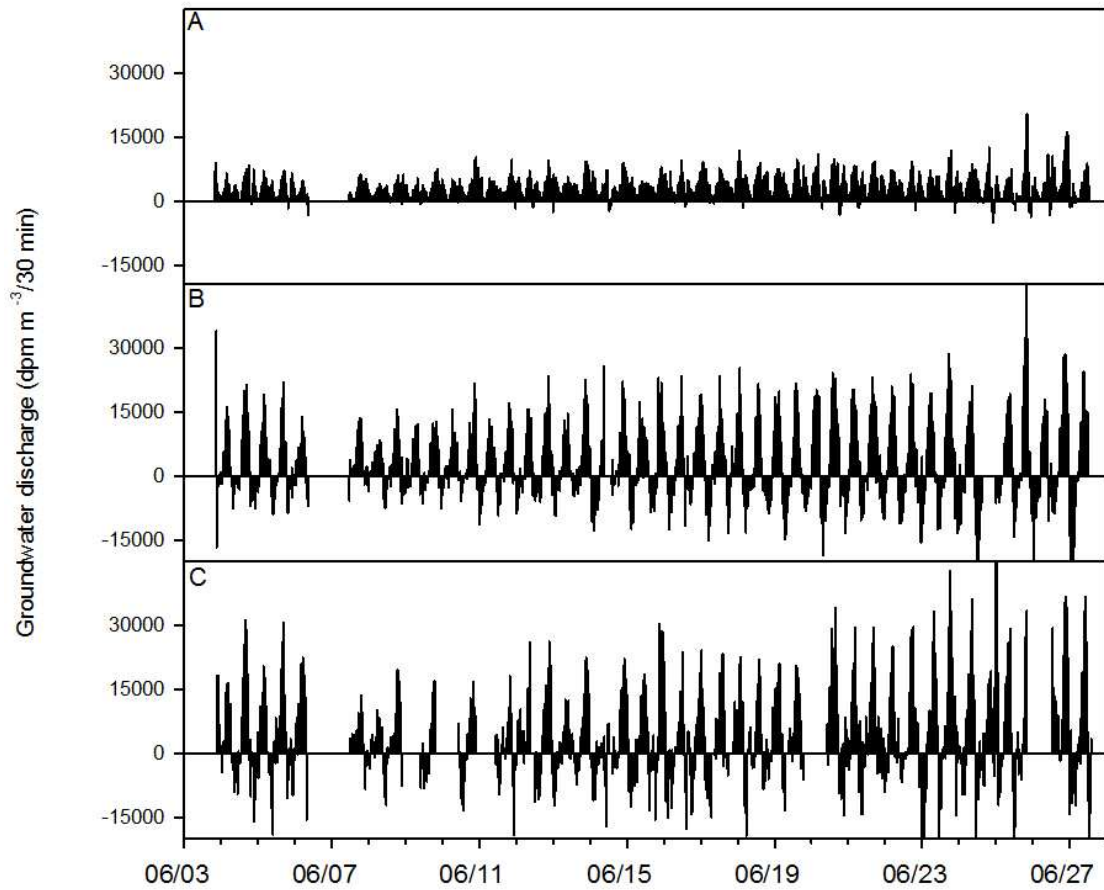


Figure 8: 30-minute interval groundwater discharge rates from the non-steady state mass balance equation at Upper Duplin (A), Central Duplin (B), and Lower Duplin (C).

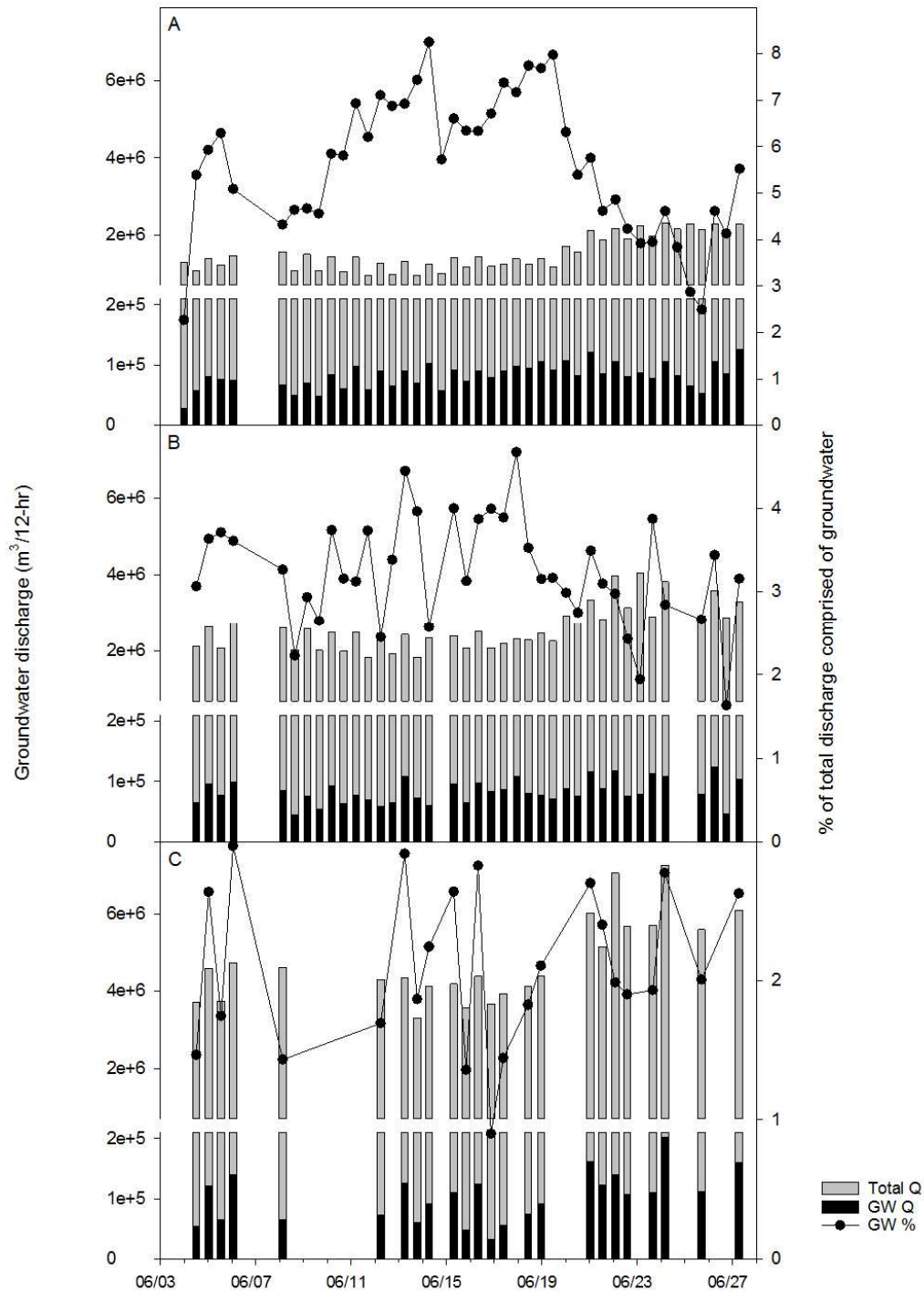


Figure 9: Total groundwater discharge from each river section over a 12 hour tidal cycle (black bars) and surface water discharge (gray bars) at Upper Duplin (A) Central Duplin (B) Lower Duplin (C). Percent groundwater composition of discharging water is shown by the line graph.

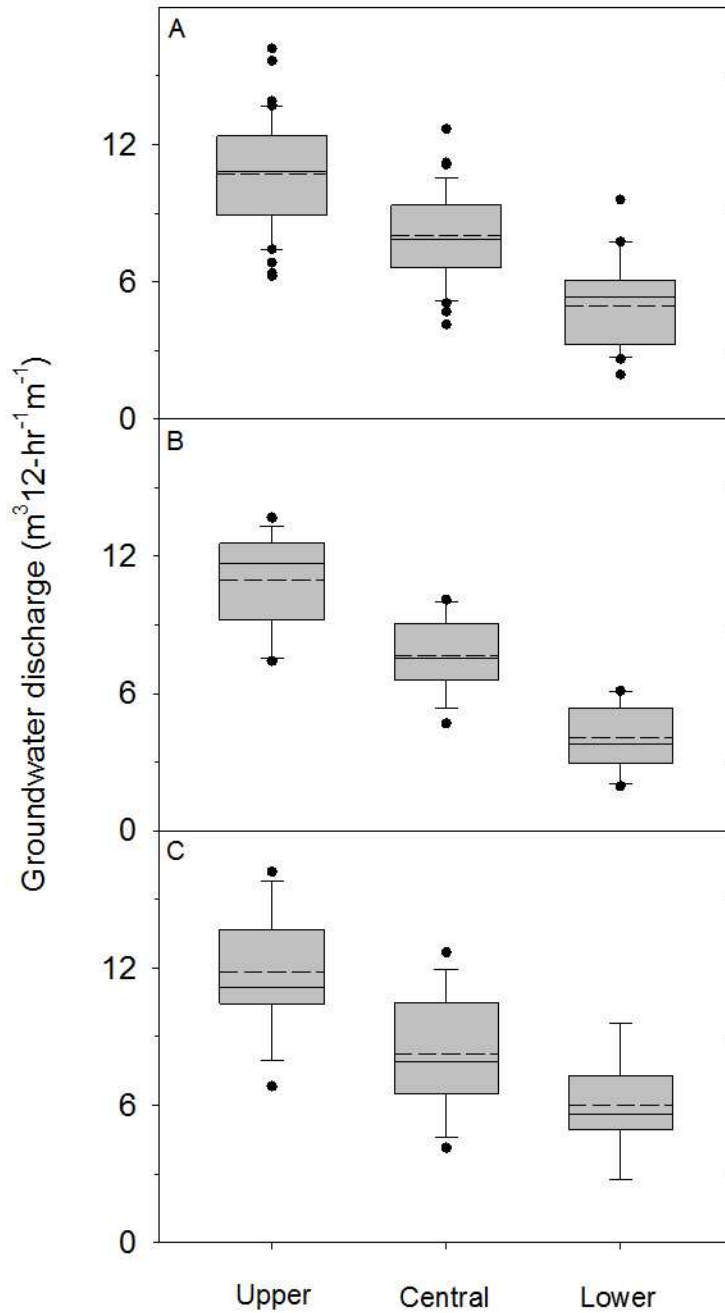


Figure 10: Total 12-hour groundwater discharge normalized to length of main channel in each section for the measurement duration (A) neap tide conditions (B) and spring tide conditions (C). Box plots show median values (solid horizontal line), mean (dashed line), 50th percentile values (box outline), 10th and 90th percentile values (whiskers), and individual outlier values (black circles).

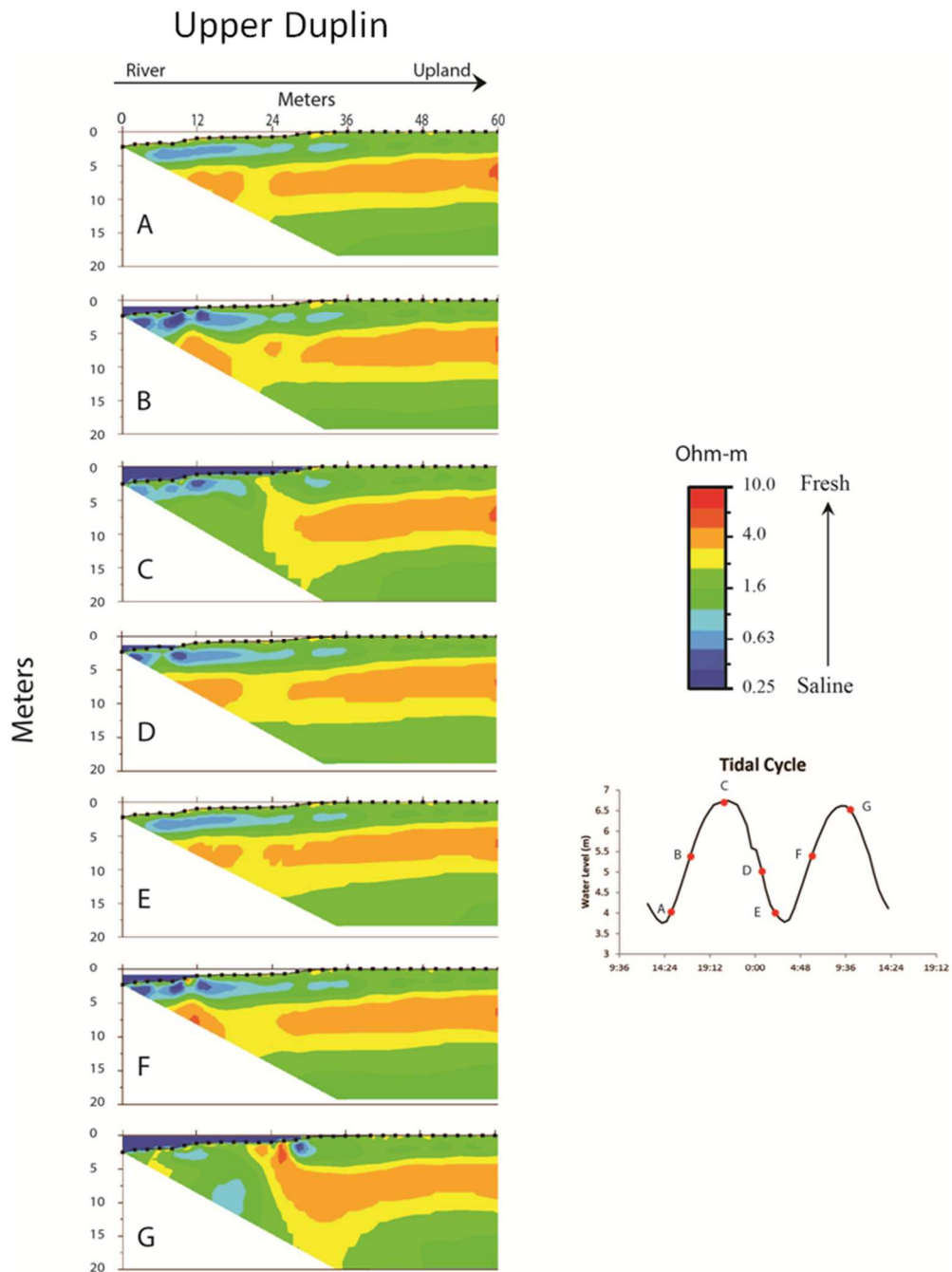


Figure 11: Stationary time series resistivity tomograms across a marsh platform at the Upper Duplin site as a function of water level.

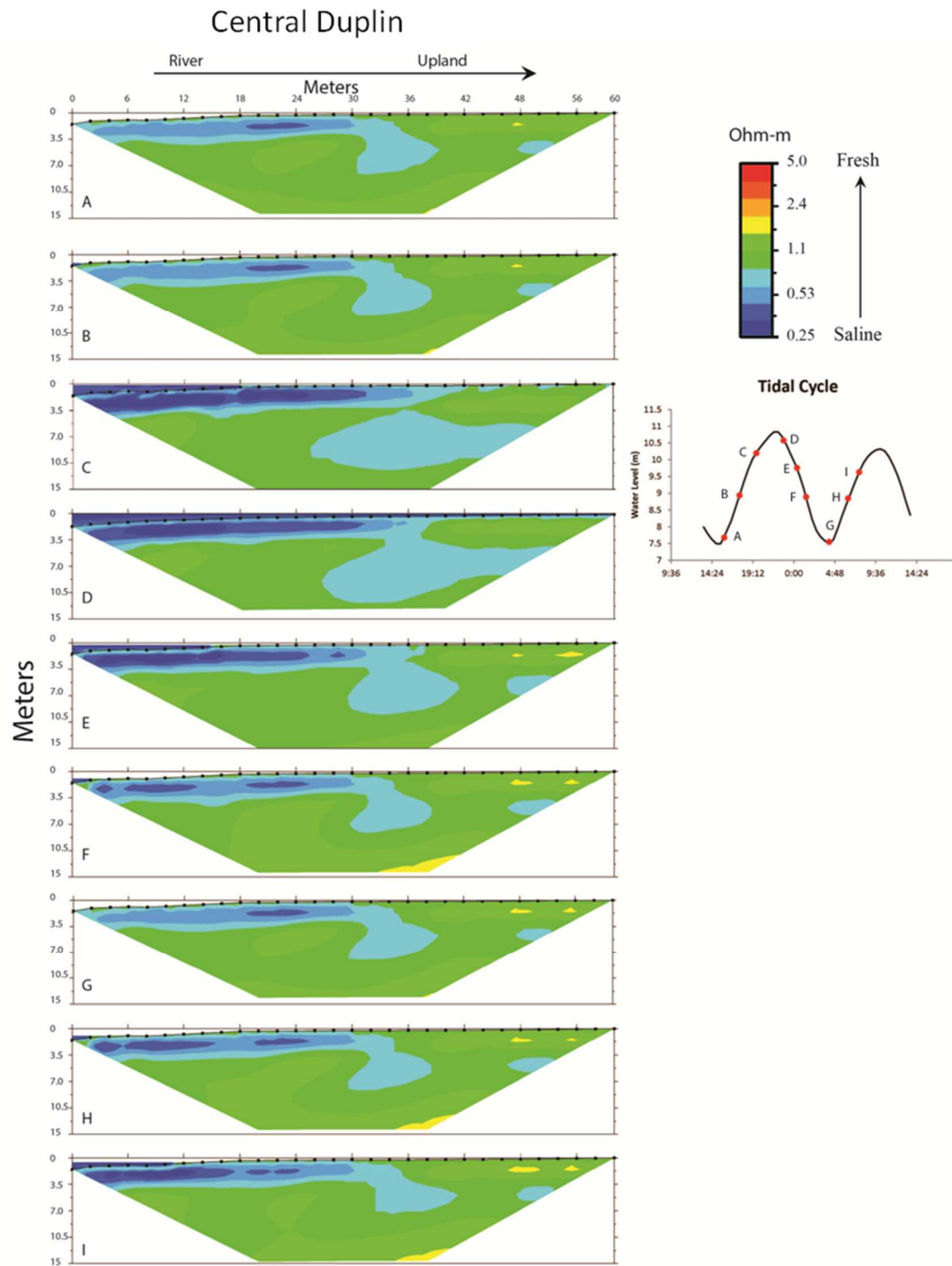


Figure 12: Time series resistivity tomograms across the marsh platform at the Central Duplin site as a function of water level.

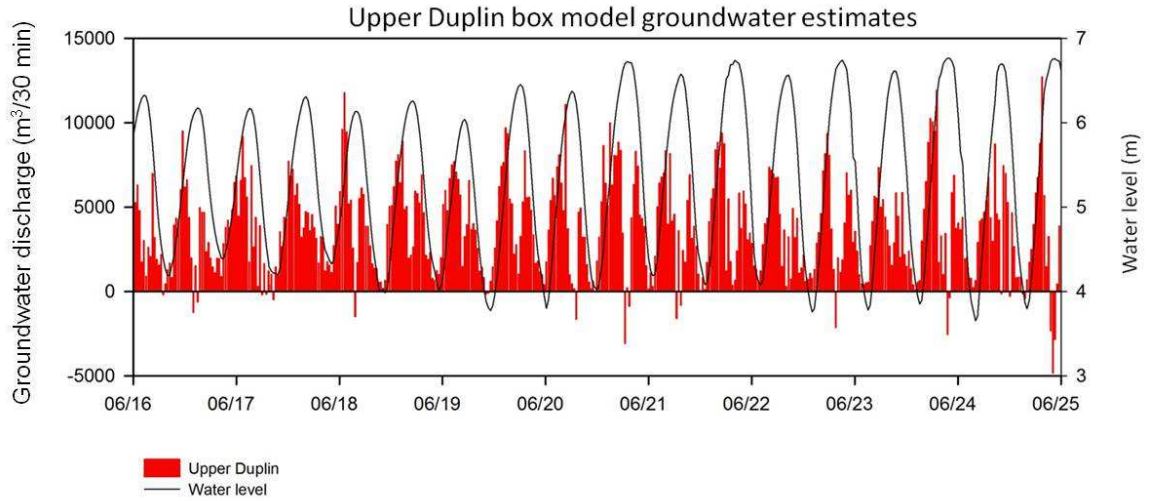


Figure 13: 30-minute interval groundwater discharge at the Upper Duplin site (red bars) corresponding to tidal stage (black lines). Maximum groundwater discharge occurs during peak tide flow.

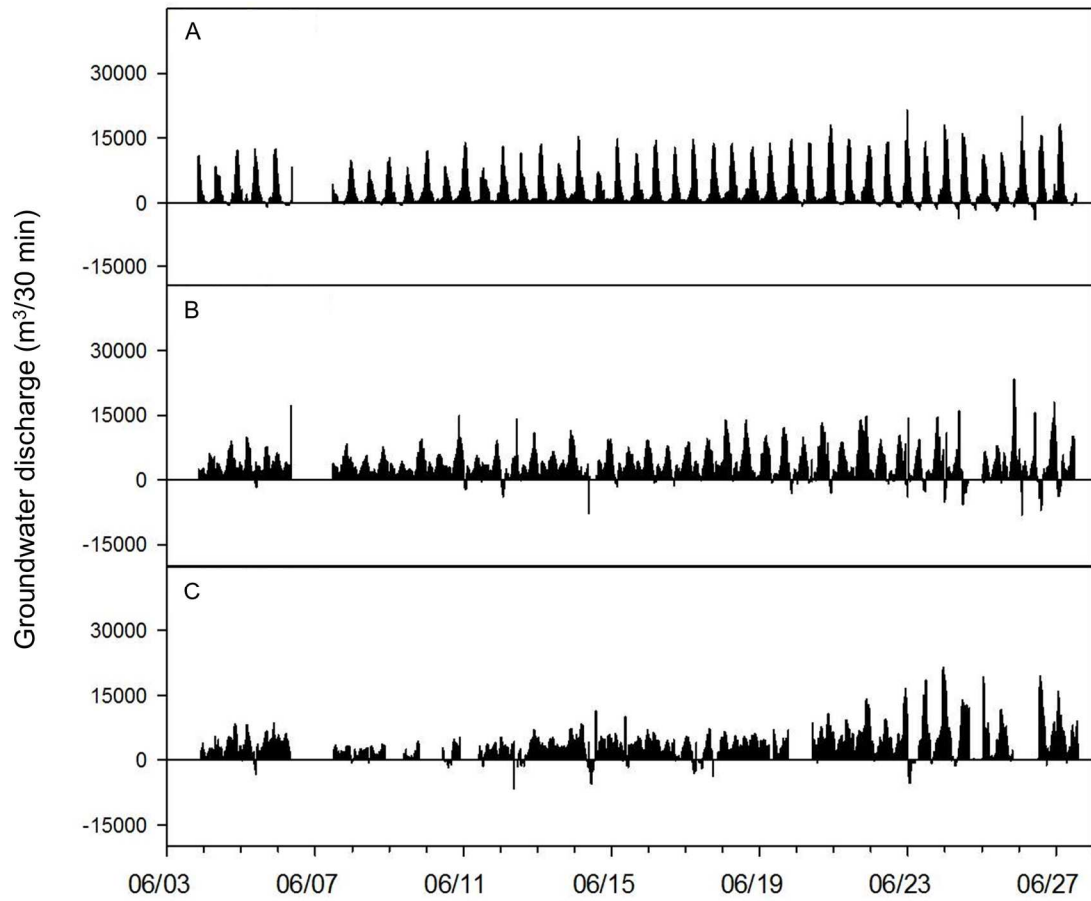


Figure 14: 30-minute groundwater discharge rate calculated from the steady-state mass balance equation for the Upper (A), Central (B), and Lower (C) Duplin sections.

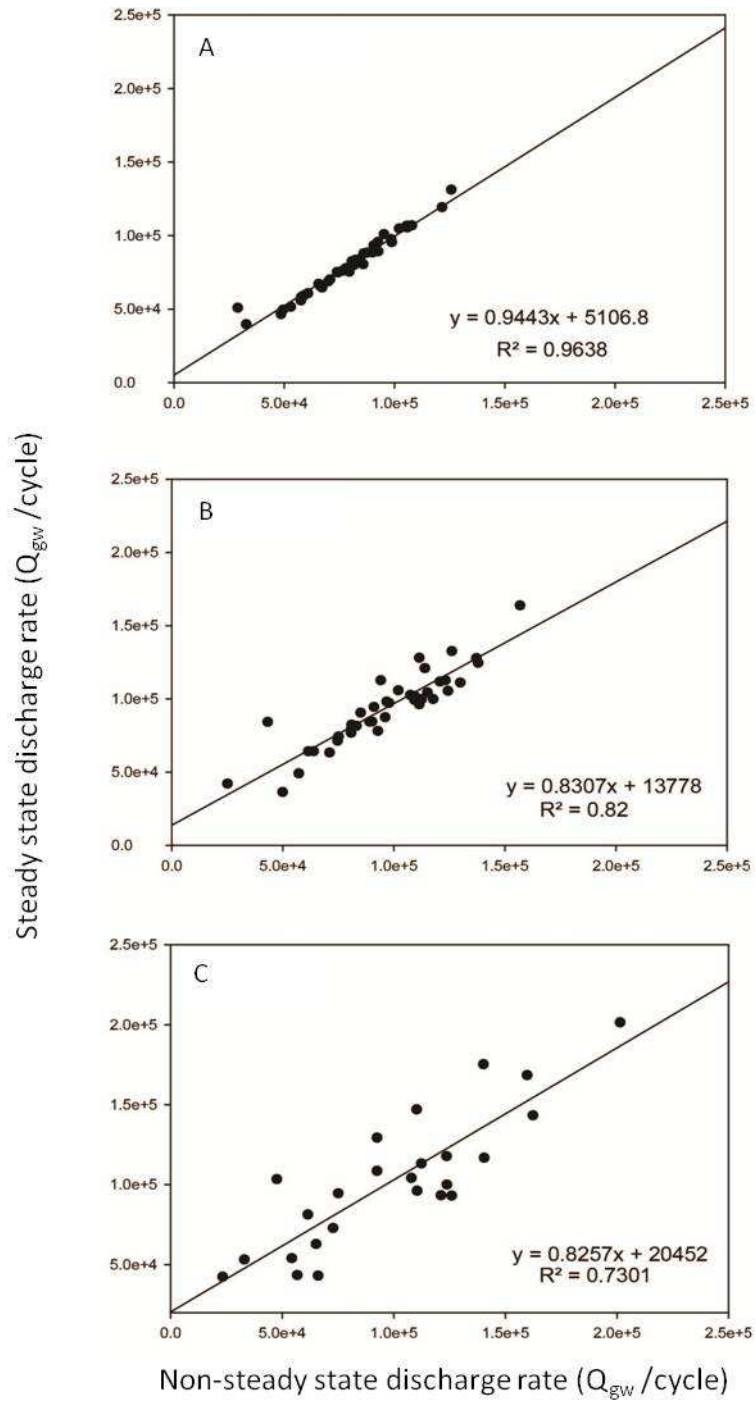


Figure 15: Comparison of the 12-hour groundwater discharge totals between the steady-state mass balance approach (y-axis) and our non-steady state mass balance approach (x-axis).

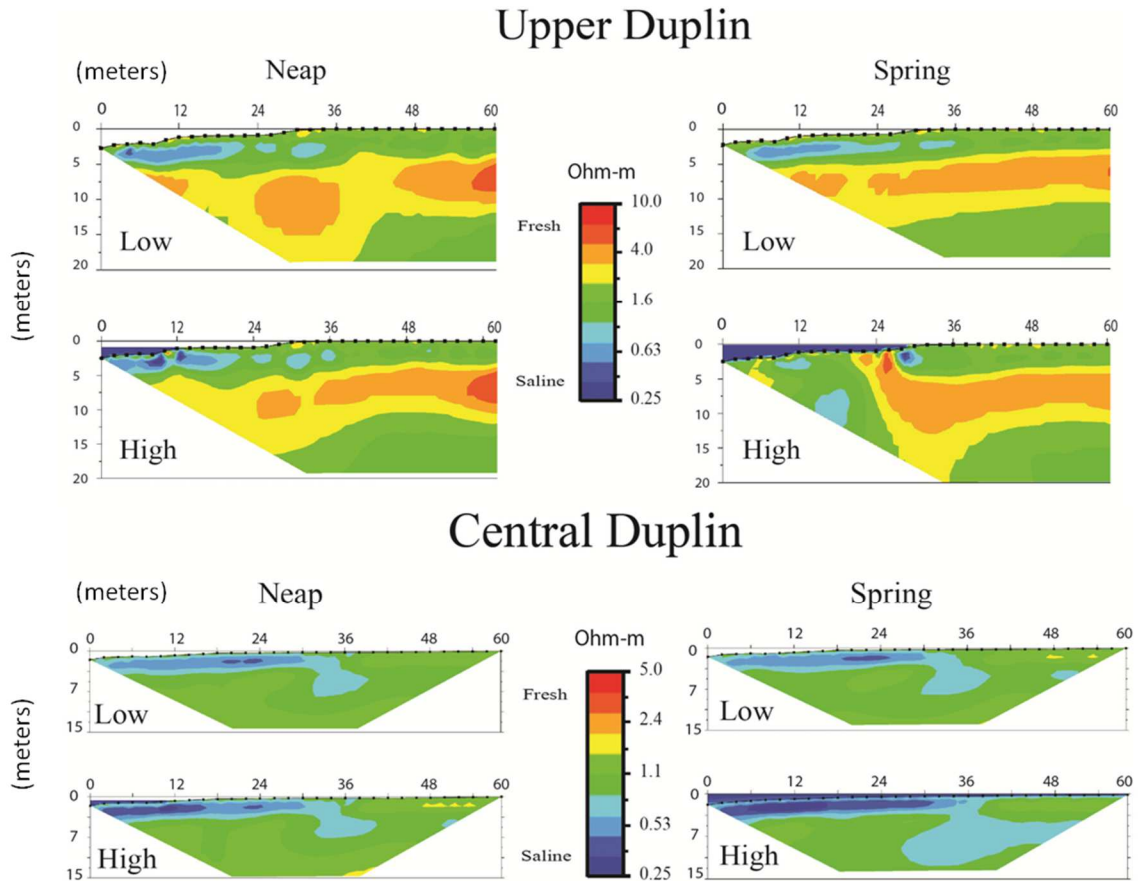


Figure 16: Upper Duplin (top) and Central Duplin (bottom) resistivity tomograms for both spring and neap time series measurements. The warm colors (red and orange) indicate higher values of resistivity signifying freshening of porewater, while cool colors (blue) indicates lower resistivity values indicating salt-water intrusion.

APPENDIX A

Supplementary radon data for the three time series radon stations:

The following tables provide water volume calculations from the Duplin River digital elevation model. The water level data and associated tidal level for each section of the river were used to determine the volume of water at specific tidal stages. This data was separated into 0.4 meter steps to create a water volume calibration curve used in the radon mass balance equation. The second set tables provide groundwater volumes and discharge rates that were calculated using the radon mass balance equation. Each table represents a section of the Duplin River, starting with the Upper Duplin section followed by the Central Duplin section, and the third table data is associated with the Lower Duplin section.

Water Volume Calculations

The water volume calculation table is labeled as follows; tidal height ranging from 0 to 3.6 meters spaced at 0.4 m intervals, water level (WL) measurements from the field deployment at each station, elevation (Elev.) is the NAVD 88 datum conversion from our water level measurement. Volume is the computed volume of water within each section of the Duplin River at the associated water level. Surface area is the computed area that water reaches at the associated tidal elevations. Depth is the average depth of water at each station based upon the water volume divided by the surface area.

Upper Duplin					
	WL (m)	Elev. (m)	Volume(m ³)	Surface Area(m ²)	Depth (Vol/SA)
Low Tide (0.0)	3.662	-1.558	225,011.3	108,319.9	2.1
0.4	4.062	-1.158	275,512.7	148,542.1	1.9
0.8	4.462	-0.758	349,118.9	233,058.9	1.5
1.2	4.862	-0.358	468,002.1	366,180.8	1.3
1.6	5.262	0.042	641,619.7	510,326.6	1.3
2	5.662	0.442	884,218.8	735,690.8	1.2
2.4	6.062	0.842	1,368,345.5	1,720,353.2	0.8
2.8	6.462	1.242	2,147,705.7	2,026,145.1	1.1
3.2	6.862	1.642	2,959,317.9	2,031,385.0	1.5
High Tide (3.6)	7.262	2.042	3,772,178.8	2,032,438.7	1.9

Central Duplin					
	WL (m)	Elev. (m)	Volume(m ³)	Surface Area(m ²)	Depth (Vol/SA)
Low Tide (0.0)	7.412	-1.598	1,419,700.1	372,550.0	3.8
0.4	7.812	-1.198	1,574,281.6	407,977.2	3.9
0.8	8.212	-0.798	1,750,994.4	478,522.1	3.7
1.2	8.612	-0.398	1,962,383.1	597,940.5	3.3
1.6	9.012	0.002	2,241,402.0	806,602.1	2.8
2	9.412	0.402	2,607,221.7	1,032,591.5	2.5
2.4	9.812	0.802	3,100,625.3	1,545,747.4	2.0
2.8	10.212	1.202	3,909,199.2	2,528,978.6	1.5
3.2	10.612	1.602	5,027,484.1	2,919,312.8	1.7
High Tide (3.6)	11.012	2.002	6,201,141.0	2,939,741.4	2.1

Lower Duplin					
	WL (m)	Elev. (m)	Volume(m ³)	Surface Area(m ²)	Depth (Vol/SA)
Low Tide (0.0)	1.411	-1.438	4,321,107.8	1,195,171.9	3.6
0.4	1.811	-1.038	4,816,531.4	1,284,689.1	3.7
0.8	2.211	-0.638	5,349,956.1	1,381,380.1	3.9
1.2	2.611	-0.238	5,921,404.8	1,481,716.5	4.0
1.6	3.011	0.162	6,537,207.0	1,609,161.5	4.1
2	3.411	0.562	7,222,351.8	1,868,317.1	3.9
2.4	3.811	0.962	8,274,285.9	4,336,760.8	1.9
2.8	4.211	1.362	10,680,196.5	6,653,495.7	1.6
3.2	4.611	1.762	13,346,386.6	6,671,114.9	2.0
High Tide (3.6)	5.011	2.162	16,016,362.2	6,677,792.5	2.4

Groundwater Calculation Table

The date column provides the date and time of the tidal cycle measurement. The m^3/cycle column is the groundwater discharge from the mass balance equation. The value displayed in the table is the integrated sum over a tidal cycle (low –low) in the m^3/cycle column. The cm/cycle column is the groundwater rate in terms of a linear velocity (cm/cycle). The calculated volume of groundwater was divided by the individual section surface area (at mean water level) provided by the Duplin River DEM. The m^2/cycle column is the flux of groundwater per tidal cycle. The total groundwater volume is divided by the average depth of each box. The $m^3/\text{m cycle}$ represents the normalization standard represented in the main body of the thesis, the groundwater discharger per meter shoreline of each individual section quantified over a tidal cycle. The last column $m^3/\text{m day}$ uses the same value as the $m^3/\text{m cycle}$ column but the total is integrated into a daily rate.

Upper Duplin:

Date	m ³ /cycle	cm/cycle	m ² /cycle	m ³ /m cycle	m ³ /m day
6/3/13 23:54	2.89E+04	9.64	1.52E+04	3.73	7.45
6/4/13 12:25	5.76E+04	19.22	3.03E+04	7.43	14.86
6/5/13 0:25	8.16E+04	27.20	4.29E+04	10.52	21.03
6/5/13 12:55	7.66E+04	25.52	4.03E+04	9.87	19.73
6/6/13 1:25	7.43E+04	24.78	3.91E+04	9.58	19.16
-	-	-	-	-	-
6/8/13 3:02	6.72E+04	22.38	3.53E+04	8.65	17.31
6/8/13 15:03	4.94E+04	16.48	2.60E+04	6.37	12.74
6/9/13 3:33	6.99E+04	23.30	3.68E+04	9.01	18.01
6/9/13 15:33	4.85E+04	16.16	2.55E+04	6.25	12.50
6/10/13 4:03	8.44E+04	28.12	4.44E+04	10.87	21.74
6/10/13 16:04	6.08E+04	20.25	3.20E+04	7.83	15.66
6/11/13 4:43	9.85E+04	32.82	5.18E+04	12.69	25.37
6/11/13 17:02	5.89E+04	19.65	3.10E+04	7.60	15.19
6/12/13 5:32	9.00E+04	30.00	4.74E+04	11.60	23.19
6/12/13 17:20	6.62E+04	22.07	3.48E+04	8.53	17.06
6/13/13 5:50	9.11E+04	30.37	4.80E+04	11.74	23.48
6/13/13 18:20	7.08E+04	23.58	3.72E+04	9.12	18.23
6/14/13 6:20	1.02E+05	34.04	5.38E+04	13.16	26.32
6/14/13 18:59	5.75E+04	19.18	3.03E+04	7.41	14.83
6/15/13 7:29	9.26E+04	30.87	4.87E+04	11.93	23.86
6/15/13 19:59	7.39E+04	24.65	3.89E+04	9.53	19.06
6/16/13 7:59	9.12E+04	30.39	4.80E+04	11.75	23.49
6/16/13 21:00	7.95E+04	26.50	4.18E+04	10.24	20.49
6/17/13 9:39	9.06E+04	30.19	4.77E+04	11.67	23.34
6/17/13 22:09	9.88E+04	32.93	5.20E+04	12.73	25.46
6/18/13 10:39	9.52E+04	31.74	5.01E+04	12.27	24.54
6/18/13 23:09	1.06E+05	35.41	5.59E+04	13.69	27.38
6/19/13 11:10	9.25E+04	30.83	4.87E+04	11.92	23.84
6/20/13 0:10	1.08E+05	35.97	5.68E+04	13.90	27.81
6/20/13 11:59	8.34E+04	27.82	4.39E+04	10.75	21.51
6/21/13 1:00	1.22E+05	40.53	6.40E+04	15.67	31.34
6/21/13 13:05	8.60E+04	28.68	4.53E+04	11.09	22.17
6/22/13 2:05	1.05E+05	35.15	5.55E+04	13.59	27.18
6/22/13 14:06	8.06E+04	26.88	4.24E+04	10.39	20.78
6/23/13 3:06	8.75E+04	29.18	4.61E+04	11.28	22.56
6/23/13 15:06	7.80E+04	26.01	4.11E+04	10.06	20.11
6/24/13 4:06	1.06E+05	35.44	5.60E+04	13.70	27.40
6/24/13 16:07	8.23E+04	27.44	4.33E+04	10.61	21.22
6/25/13 5:07	6.56E+04	21.86	3.45E+04	8.45	16.90
6/25/13 16:52	5.30E+04	17.66	2.79E+04	6.83	13.65
6/26/13 5:52	1.06E+05	35.26	5.57E+04	13.63	27.26
6/26/13 17:23	8.58E+04	28.60	4.52E+04	11.06	22.11
6/27/13 6:53	1.26E+05	41.92	6.62E+04	16.21	32.41
Tidal cycle average	8.21E+04	27.36	4.32E+04	10.58	
Average day-1	1.64E+05	54.73	8.64E+04	21.16	21.16

Central Duplin:

Date	m ³ /cycle	cm/cycle	m ² /cycle	m ³ /m cycle	m ³ /m day
-	-	-	-	-	-
6/4/13 12:00	7.70E+04	16.63	2.15E+04	6.08	12.17
6/5/13 0:30	1.12E+05	24.27	3.14E+04	8.88	17.76
6/5/13 12:46	9.28E+04	20.05	2.60E+04	7.34	14.68
6/6/13 1:17	1.18E+05	25.54	3.31E+04	9.35	18.69
-	-	-	-	-	-
6/8/13 3:04	1.20E+05	25.84	3.35E+04	9.46	18.92
6/8/13 15:04	6.56E+04	14.18	1.84E+04	5.19	10.38
6/9/13 3:35	9.83E+04	21.24	2.75E+04	7.77	15.55
6/9/13 15:42	5.92E+04	12.80	1.66E+04	4.68	9.37
6/10/13 4:12	1.26E+05	27.17	3.52E+04	9.94	19.89
6/10/13 16:12	8.53E+04	18.43	2.39E+04	6.74	13.49
6/11/13 4:43	1.10E+05	23.78	3.08E+04	8.70	17.40
6/11/13 16:39	8.31E+04	17.95	2.32E+04	6.57	13.14
6/12/13 5:45	7.37E+04	15.92	2.06E+04	5.83	11.65
6/12/13 17:15	7.77E+04	16.79	2.17E+04	6.14	12.29
6/13/13 6:15	1.28E+05	27.57	3.57E+04	10.09	20.18
6/13/13 18:16	9.38E+04	20.26	2.62E+04	7.42	14.83
6/14/13 6:16	9.70E+04	20.95	2.71E+04	7.67	15.33
-	-	-	-	-	-
6/15/13 7:20	1.15E+05	24.75	3.20E+04	9.06	18.11
6/15/13 20:29	8.87E+04	19.15	2.48E+04	7.01	14.02
6/16/13 8:20	1.16E+05	24.99	3.24E+04	9.15	18.29
6/16/13 20:54	9.56E+04	20.66	2.67E+04	7.56	15.12
6/17/13 9:24	1.05E+05	22.72	2.94E+04	8.32	16.63
6/17/13 22:25	1.33E+05	28.77	3.72E+04	10.53	21.05
6/18/13 10:25	1.14E+05	24.73	3.20E+04	9.05	18.10
6/18/13 23:25	1.17E+05	25.24	3.27E+04	9.24	18.47
6/19/13 10:56	9.95E+04	21.50	2.78E+04	7.87	15.74
6/20/13 0:26	1.12E+05	24.28	3.14E+04	8.89	17.77
6/20/13 12:17	8.39E+04	18.13	2.35E+04	6.64	13.27
6/21/13 1:17	1.42E+05	30.62	3.96E+04	11.20	22.41
6/21/13 13:18	1.01E+05	21.78	2.82E+04	7.97	15.94
6/22/13 1:48	1.60E+05	34.64	4.48E+04	12.68	25.35
6/22/13 14:24	8.38E+04	18.10	2.34E+04	6.62	13.25
6/23/13 2:54	8.85E+04	19.12	2.48E+04	7.00	13.99
6/23/13 15:24	6.40E+04	13.83	1.79E+04	5.06	10.12
6/24/13 4:09	1.24E+05	26.82	3.47E+04	9.81	19.63
-	-	-	-	-	-
6/25/13 16:41	7.80E+04	16.86	2.18E+04	6.17	12.34
-	-	-	-	-	-
6/26/13 5:53	1.41E+05	30.38	3.93E+04	11.12	22.23
6/26/13 17:42	5.23E+04	11.30	1.46E+04	4.14	8.27
6/27/13 6:43	1.30E+05	28.02	3.63E+04	10.25	20.51
Tidal cycle average	1.02E+05	21.94	2.84E+04	8.03	
Daily Average	2.03E+05	43.88	5.68E+04	16.06	16.06

Lower Duplin:

Date	m ³ /cycle	cm/cycle	m ² /cycle	m ³ /m cycle	m ³ /m day
-	-	-	-	-	-
6/4/13 12:02	6.55E+04	5.12	2.20E+04	5.24	5.69601
6/5/13 0:32	1.35E+05	10.58	4.55E+04	10.83	11.7765
6/5/13 12:32	7.81E+04	6.11	2.62E+04	6.25	6.79433
6/6/13 1:03	1.56E+05	12.16	5.23E+04	12.45	13.5358
-	-	-	-	-	-
6/8/13 3:09	7.55E+04	5.90	2.54E+04	6.04	6.56688
-	-	-	-	-	-
-	-	-	-	-	-
-	-	-	-	-	-
-	-	-	-	-	-
-	-	-	-	-	-
-	-	-	-	-	-
6/12/13 5:38	8.38E+04	6.55	2.82E+04	6.71	7.29033
-	-	-	-	-	-
6/13/13 5:51	1.41E+05	10.99	4.73E+04	11.25	12.2327
6/13/13 18:21	7.43E+04	5.80	2.50E+04	5.94	6.45904
6/14/13 6:21	1.05E+05	8.19	3.52E+04	8.39	9.11986
-	-	-	-	-	-
6/15/13 7:24	1.24E+05	9.67	4.16E+04	9.91	10.767
6/15/13 19:54	6.03E+04	4.71	2.03E+04	4.82	5.24297
6/16/13 7:54	1.37E+05	10.70	4.60E+04	10.96	11.9081
6/16/13 20:55	4.47E+04	3.49	1.50E+04	3.57	3.88497
6/17/13 9:20	6.81E+04	5.32	2.29E+04	5.45	5.9201
-	-	-	-	-	-
6/18/13 10:15	8.77E+04	6.86	2.95E+04	7.02	7.62979
6/18/13 23:15	1.05E+05	8.17	3.51E+04	8.37	9.09448
-	-	-	-	-	-
-	-	-	-	-	-
-	-	-	-	-	-
6/21/13 0:58	1.78E+05	13.93	5.99E+04	14.26	15.5017
6/21/13 12:58	1.39E+05	10.82	4.65E+04	11.08	12.0457
6/22/13 1:58	1.57E+05	12.24	5.26E+04	12.54	13.625
6/22/13 13:59	1.23E+05	9.58	4.12E+04	9.81	10.6581
6/23/13 2:59	6.30E+04	4.92	2.12E+04	5.04	5.47975
-	-	-	-	-	-
6/24/13 3:46	2.21E+05	17.23	7.41E+04	17.64	19.1766
6/24/13 15:46	1.25E+05	9.80	4.22E+04	10.04	10.9114
6/25/13 16:47	1.29E+05	10.07	4.33E+04	10.31	11.2072
-	-	-	-	-	-
-	-	-	-	-	-
-	-	-	-	-	-
6/27/13 6:24	1.77E+05	13.85	5.95E+04	14.18	15.4089
Tidal cycle average	1.14E+05	8.91	3.83E+04	9.12	
Daily Average	2.28E+05	17.82	7.66E+04	18.25	18.25

APPENDIX B

Resistivity:

In addition to the presented resistivity data, multiple tomograms were taken throughout the field measurement. Listed below describes each time series electrical resistivity measurement with a figure and appropriate interpretation. We were unable to directly compare the sites because of the geological differences between the two measurement sites. The presented data shows how pore fluid resistive properties may vary in two separate geologic formations. As stated in the methods section of the main body, the time series approach of electrical resistivity allows us to omit geologic formations as a source for changes in resistivity over the measurement interval.

1. *Upper Duplin:*

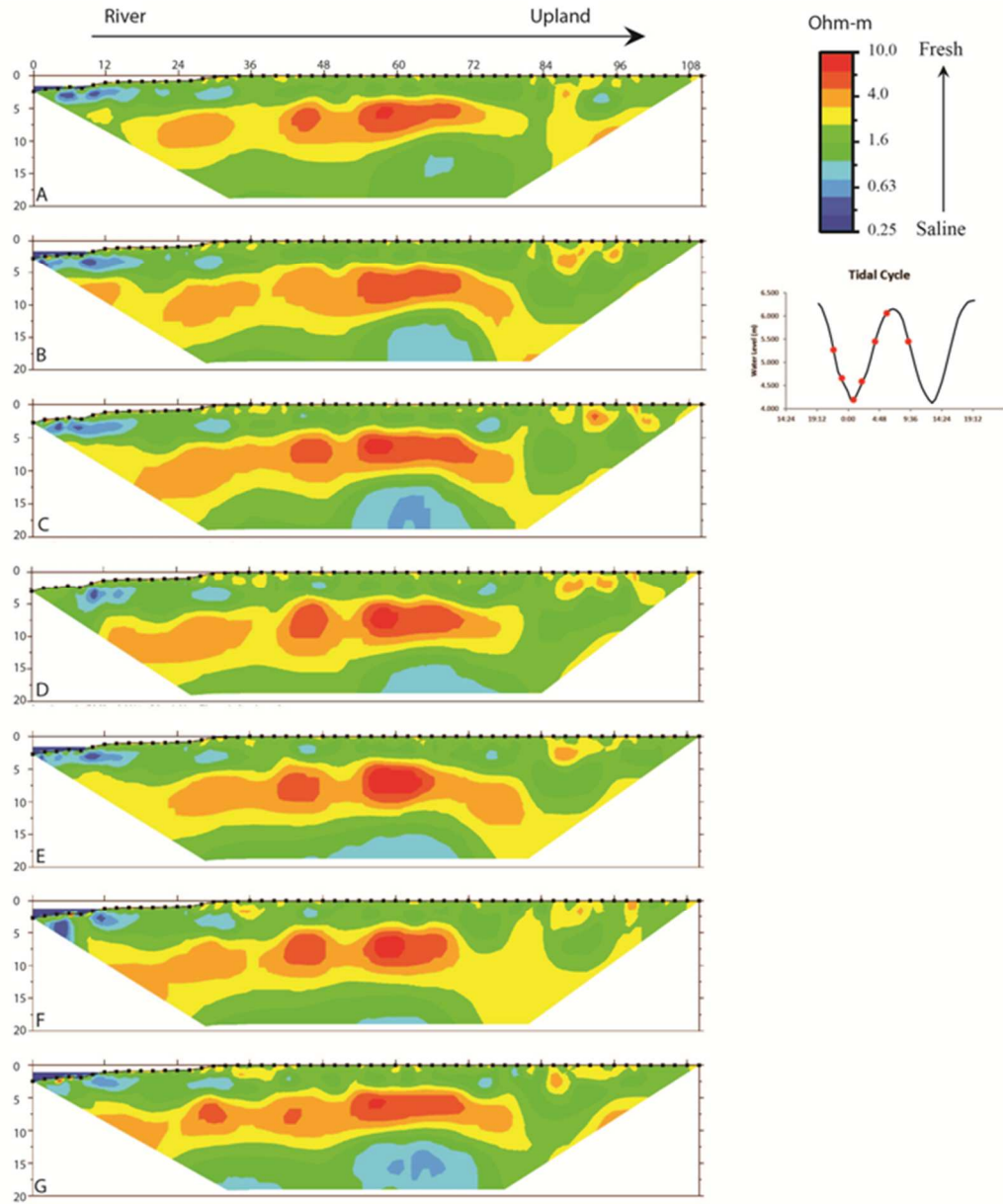
The total length of each transect was 108 meters that expand across the hammock upland, adjacent fringe marsh, and 6 meters into the Duplin River main channel. A two-layer system was recognized as signified by the contrasting resistivity signatures between the upper (<5 m) and mid (5-10 m) and lower (>15 m) depth zones of all tomograms at the Upper Duplin site. Resistivity values 1-2 Ohm-meters in the upper zone were most likely due to a combination of organic mud and sandy soil mixture. This is confirmed by our shallow marsh vibracores. The self-contained freshwater lens as described by Schultz and Ruppel (2002). The mid layer of higher resistivity (2-10 Ohm-meters) can be attributed to the hammock's self contained freshwater as described by Schultz and Ruppel (2002). The lower zone consisted of low resistivity (<2 ohm-meters) most likely associated with a shift in sediment type and increased saline pore fluid from the Dupuit – Ghyben-Herzberg theory that describes a lens like morphology of freshwater aquifers

beneath barrier islands. This could also be linked to the clay layer aquifer boundary. Geophysical data on Sapelo Island showed an asymmetrical lens and a freshwater-saltwater interface on the back barrier estuary at depths greater than 10 meters (Schultz et al., 2007). We can assume our measurements portray a good representation of the subsurface fluid interaction based upon the extensive geophysical archive of Sapelo Island. For our instance, we were more focused on the shallow water freshwater-saltwater interaction within the marsh-zone located on the left side of all tomograms.

1.1 Upper Duplin 060413:

A total of 7 tomograms were taken over an 18 hour measurement period in neap tide conditions. For our purpose, the regions of the tomogram will be described as marsh zone (0-30 meters) and upland zone (31-108 meters) along the horizontal axis. During an ebb tide (A-D) there is an increase in resistive properties within the shallow marsh zone shown by the reduced intensity of the cooler (blues) coloration. This was most likely a product of fluid flushing out of the marsh system and the introduction of fresher water mixed into the porewater from the surficial hammock aquifer. Panel D was during the next flood tide, however there was increased resistivity (freshening) in the marsh zone due to the hydraulic gradient in favor of discharge. The following panels (E-F) describe marsh zone recharge of saline water from the Duplin River. Well developed areas of low resistivity infer saline water has replaced brackish water (D through F). As the tide fell (G) we again saw a freshening effect in the shallow marsh zone with increased resistivity (shrinking area and intensity of blue coloration). Upland characteristics were primary constant throughout the measurement. The highest resistivities were between 45 and 70 meters (horizontal) and 5-10m (depth), which was a good representation of the center of the hammock and the freshwater lens maximum.

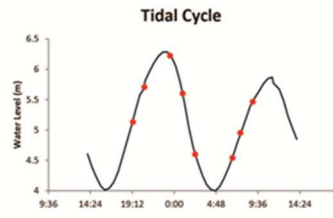
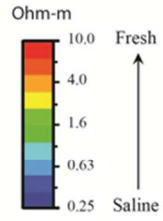
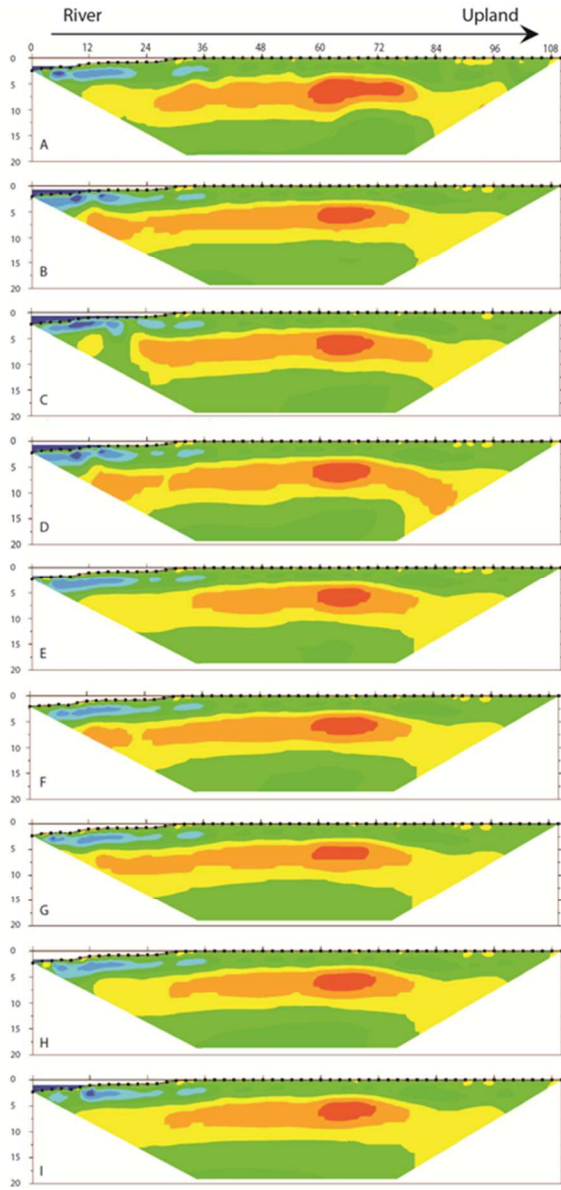
Upper Duplin 060413



1.2 Upper Duplin 061013:

A total of 9 tomograms were taken over a 24 hour measurement period in spring tide conditions. For our purpose, the regions of the tomogram will be described as marsh zone (0-30 meters) and upland zone (31-108 meters) along the horizontal axis. The initial flood tide (A-C) we see a clear zone of saline porewater (cool colors) that extends almost to the upland boarder (B and C). Panel C showed vertical migration and bulging of a high resistive zone around the 24 meter mark. This may be a result of saline flood waters squeezing the freshwater lens of the hammock in the vertical direction and forcing fresher water to the surface. During the ebb tide (C-E) there was an increase in resistivity within the shallow marsh zone shown by the reduced intensity and area of the blue coloration. This was most likely a product of fluid flushing out of the marsh system allowing fresher water mixing into the porewater from the surficial hammock aquifer. Panel F was the next flood tide, surface waters had not infiltrated the marsh system and the terrestrial hydraulic gradient was driving pore fluid towards the main river channel. The following panels (H and I) show marsh zone recharge of saline water from the Duplin River because low resistivity was seen in the shallow marsh zone. Upland characteristics stayed constant throughout the measurement. The highest resistivities were between 55 and 75 meters (horizontal) and 5-10 meters (depth), which was a good representation of the center of the hammock freshwater source.

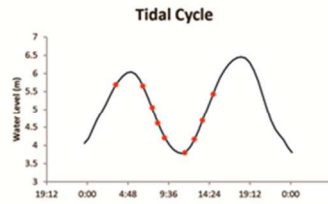
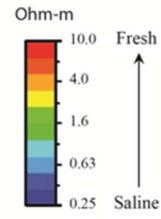
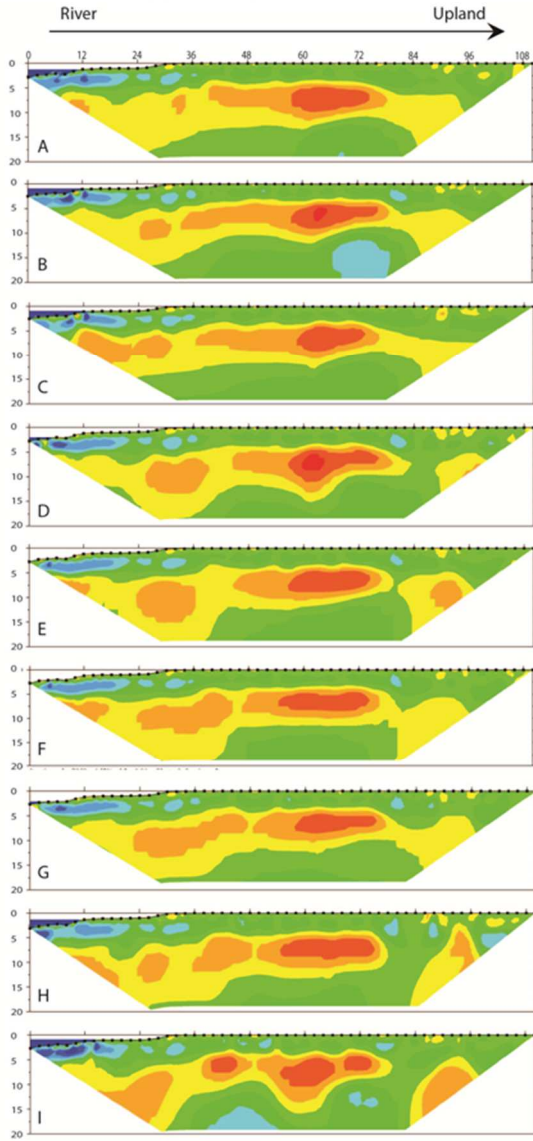
Upper Duplin 061013



1.3 Upper Duplin 061813:

A total of 9 tomograms were taken over an 18 hour measurement period in neap tide conditions. For our purpose, the regions of the tomogram will be described as marsh zone (0-30 meters) and upland zone (31-108 meters) along the horizontal axis. The initial ebb tide (B-E) showed an increase in resistive properties within the shallow marsh zone shown by the reduced intensity of the cool (blues) coloration. This was most likely a product of fluid flushing out of the marsh system and the introduction of fresher water mixing into the porewater from the surficial hammock aquifer. The patches of low resistivity in the shallow subsurface (>5 m) during the ebb tide may be linked to accelerated evapotranspiration during the summer conditions in the southeastern United States, leading to increased porewater salinity when the marsh was not inundated with water. However, the overall trend was still a “freshening” effect in the pore fluid. The following flood tide (F-G) show increased resistivity in the shallow marsh due to saline river water recharge into the pore space. Upland characteristics primary stay constant throughout the measurement. The highest resistivities were between 55 and 75 meters (horizontal) and 5-10 meters (depth), which was a good representation of the center of the hammock freshwater source.

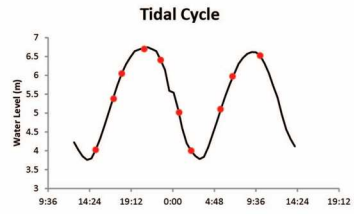
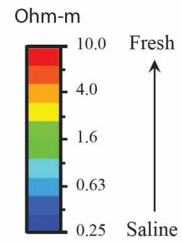
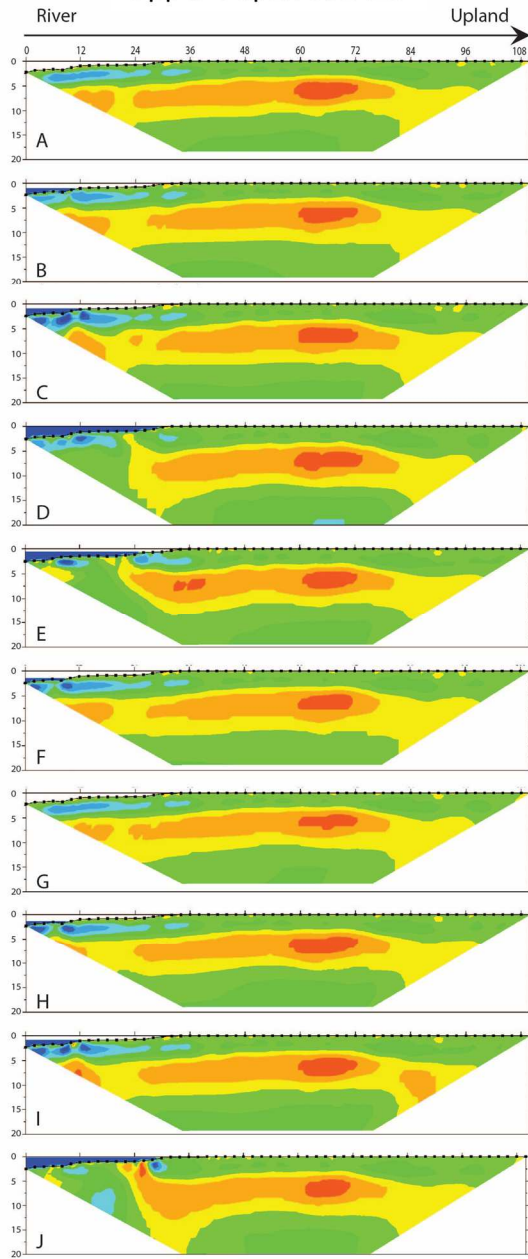
Upper Duplin 061813



1.4 Upper Duplin 062413:

A total of 10 tomograms were taken in a 24 hour measurement period in spring tide conditions. For our purpose, the regions of the tomogram will be described as marsh zone (0-30 meters) and upland zone (31-108 meters) along the horizontal axis. During this measurement we experienced unusually large tidal amplitude. The duration of each tomogram was about 90 minutes for completion. The initial flood tide (A-D) we saw a clear zone of saline intrusion in the upper marsh (expansion of low resistive zone (cool colors)). In panel C we saw a higher resistivity area around 12m. The following panels (D and E) show the development into a zone of high resistivity that migrated towards the surface. On the ebb tide (E-G) there was evidence of freshening in the marsh surface. The second flood tide, panels (H-J) show the same succession of events as describe earlier in panels (A-D) of saline intrusion and the high resistive layer extending to the surface around 24 meters. The conditions happening in successive tides indicated that this was a regular process during high spring tides. The area of lower resistivity towards the river could represent salt wedge conditions for density driven separation between the fluids. Also, the hammock is surrounded by water, and the tidal pressure may be squeezing the freshwater lens and forcing vertical migration. These processes help explain what we have seen in the time series tomograms. The developing stages of what we saw on 6/24 were also seen and describe on the previous spring tide 6/10. The new moon and full moon spring tides were substantially different in tide amplitude, this could explain why we only saw a high resistive bulge develop during the 6/10 measurement.

Upper Duplin 062413



1.5 Spring-Neap differences:

Between the four measurement events there are some consistencies within the tomograms. The spring tide measurements had a greater tidal influence in the marsh zone and the mid depth high resistive layer appeared to be more uniform in the upland while the marsh zone portion fluctuated directly with the tidal phase. Neap tide tomograms portrayed more variable conditions of the high resistive layer in both the vertical and horizontal direction in the upland zone. The shallow marsh zone resistive properties were in-phase with water level, but the differences were not as drastic as seen during spring tide measurements. We speculate this may be a correlation between the hammock hydraulic gradient and tidal elevation on a fortnightly scale. Neap conditions had smaller tidal amplitudes and reduced marsh infiltration and limited flushing. This could have allowed for greater horizontal migration of freshwater towards the main river channel. Differences on the longer scale allude to a dynamic boundary layer between fresh and saline water.

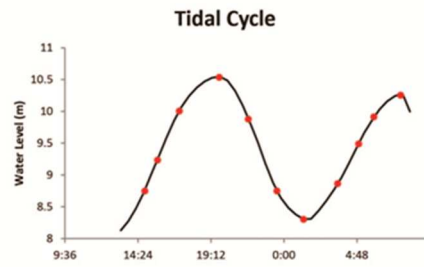
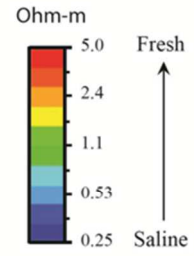
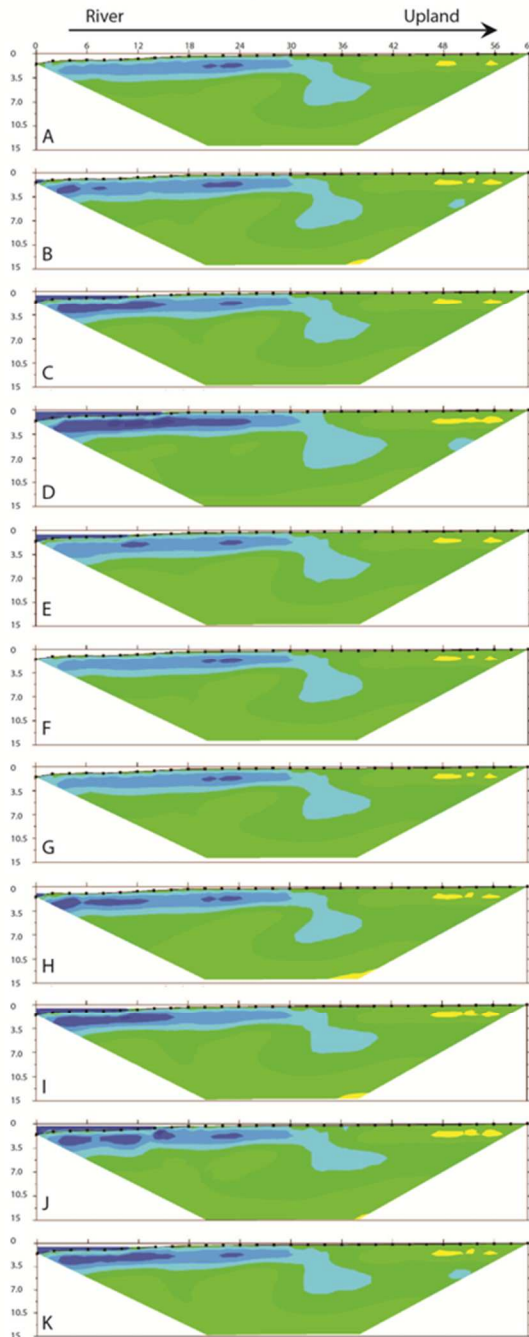
2. Central Duplin:

The total length of each transect was 60 meters that expand across the main island upland, adjacent fringe marsh, and 6 meters into the Duplin River main channel. The region was defined as a single layer system. A thick layer of marsh material (0-30 m horizontal) overlaid a uniform layer of main island sand lithology. This zone was a short fringing marsh that had a low level of relief that transition into island sands. 30-60m horizontal was a transition zone from high marsh to mainland upland sediment type. All tomograms showed an over-top “saline tongue” between 30 and 36 meters at all times as an indication of the transition between marsh sediment, and island lithology. All tomograms have a distinct saline (cool colors) signature in the shallow marsh zone. This was verified with shallow sediment cores (2m) and porewater salinity measurements at 12 and 24 meters distance from the river channel.

2.1 Central Duplin 060613:

A total of 11 tomograms were selected over a 24 hour measurement period in neap tide conditions. The initial flood tide (A-D) the “saline tongue” grows in size and there was increased intensity cooler colors as an indication of saline water intrusion. Panels (E-G) showed ebb tide freshening of the shallow marsh zone as indicated by the reduced intensity of cool colors and shrinking of the “saline tongue”. The successive flood tide resembles the description from (A-D) but the intensity of the saline intrusion was less prevalent, most likely due to the reduced tidal amplitude. In all panels there was a small shallow zone of higher resistivity near the up land (42-60 m). This area could be accredited the surficial island aquifer or sediment transition, however, no porewater measurements were taken.

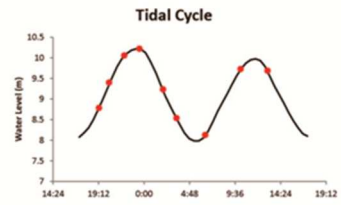
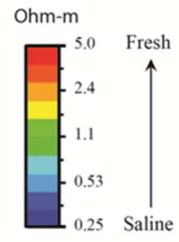
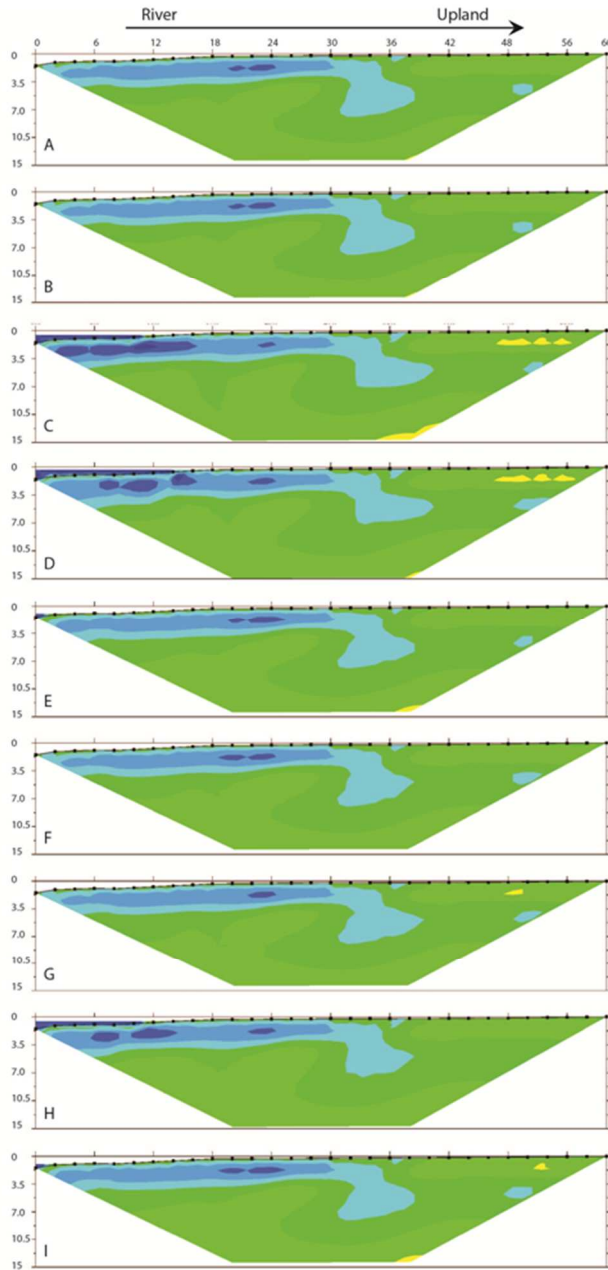
Central Duplin 060613



2.2 Central Duplin 061113:

A total of 9 tomograms were selected over a 24 hour measurement period on spring tide conditions. The initial flood tide (A-D) the “saline tongue” shifts inland and there was decreased resistivity as an indication of saline water intrusion. Panels (E-G) showed ebb tide freshening of the shallow marsh zone as indicated by the reduced intensity of cool colors and shrinking of the “saline tongue”. The successive flood tide resembled the description from (A-D) but the intensity of the saline intrusion was less prevalent, most likely due to the reduced tidal amplitude. Again, all panels show there was a small shallow zone of slightly higher resistivity near the up land (42-60 m) as possible island aquifer or sediment transition.

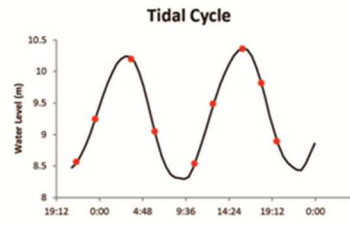
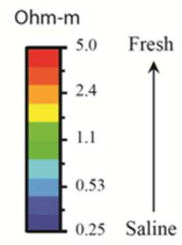
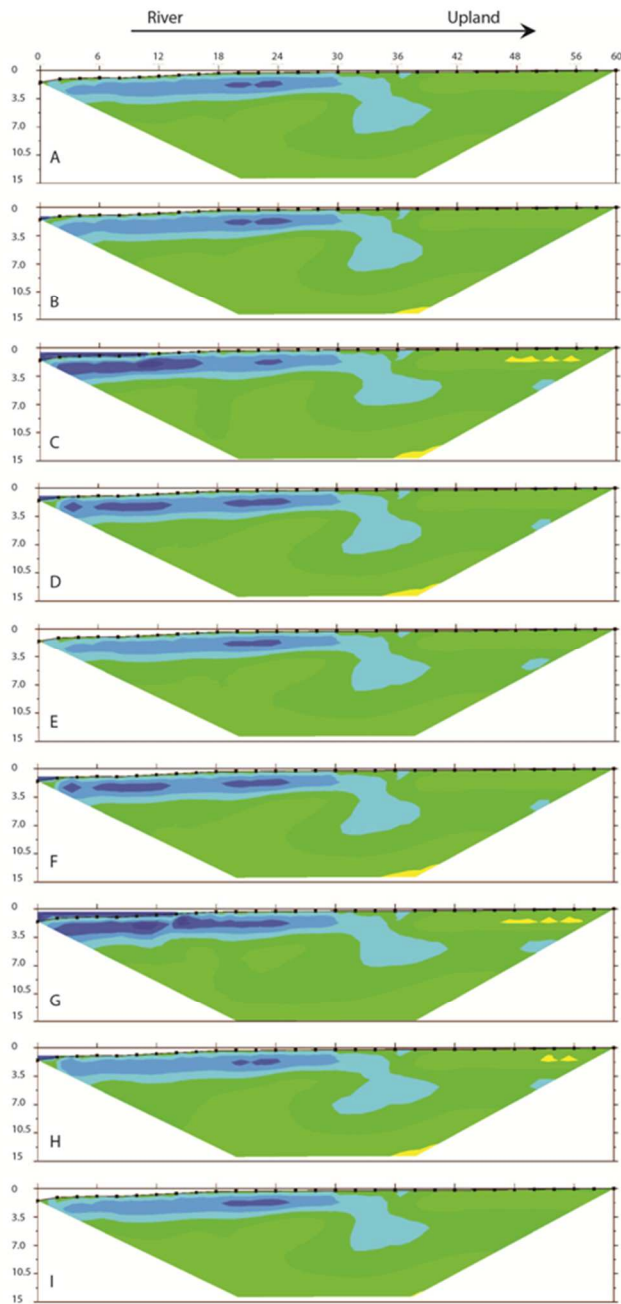
Central Duplin 061113



2.3 Central Duplin 061813:

A total of 9 tomograms were selected over a 24 hour measurement period in spring tide conditions. The initial flood tide (A-C) the “saline tongue” shifts inland and there was decreased resistivity (cooler colors) as an indication of saline water intrusion. Panels (D-E) showed freshening of the shallow marsh zone as indicated by the reduced intensity of cool colors and shrinking of the “saline tongue”. Panel E was taken during the successive flood, but indicated freshening of the pore fluid that implied terrestrial hydraulic gradient may still be a dominant force. The next flood tide resembles the description from (A-C) but the intensity of the saline intrusion is greater, most likely due to the increased tidal amplitude. In panels (C, G and H) there was a small shallow zone of slightly higher resistivity near the up land (42-60 m).

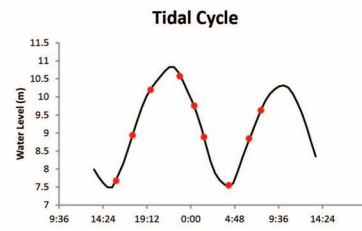
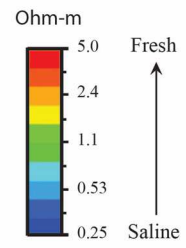
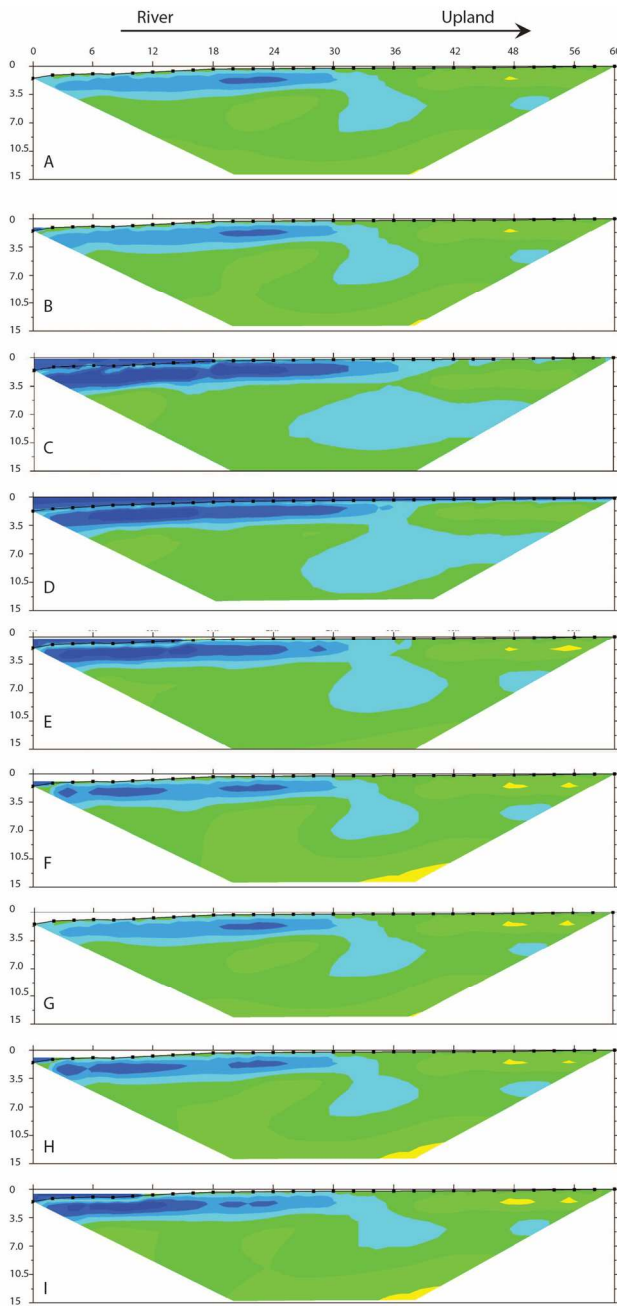
Central Duplin 061813



2.4 Central Duplin 062413:

A total of 9 tomograms were selected over a 24 hour measurement period in spring tide conditions. The initial flood tide (A-D) there was intense saline intrusion as depicted with the large areas of low resistivity. The “saline tongue” shifts inland and was significantly larger (C and D) and appeared to connect to the small low resistive area near the upland that was seen in panels A and B. Ebb tide freshening of the shallow marsh zone was indicated by the reduced intensity of cool colors and shrinking of the “saline tongue” (E-G). The successive flood tide resembles the description from (A-D) but the intensity of the saline intrusion is less prevalent, most likely due to the reduced tidal amplitude. In all panels except (C) there was a small shallow zone of slightly higher resistivity near the upland (42-60 m). All tomograms except (H) display an area of low resistivity near the upland; during the high tide (panel C and D) this zone was connected with the saline tongue. These are similar results that were seen in the previous tomograms.

Central Duplin 062413



2.5 Spring – Neap Conditions:

The intensity of saline intrusion was increased during spring tides because of overtop infiltration of saline river water. The new moon spring tide was substantially larger than any other measurement that resulted in complete inundation of the measurement domain. This may have played a role in the saline intensity recorded during the measurement. The intensity of the “saline tongue” feature was amplified during spring conditions.

3. Conclusions and Recommendations:

The measurement sites had very different resistive properties, but both sites indicated increased saline intrusion during periods of spring tide. Upper Duplin showed a more dynamic system with greater horizontal and vertical resistivity differences over a tidal cycle and fortnightly timescales. This may be due to the small surficial aquifer of a hammock setting, and provides insight to small island aquifer characteristics and their potential interactions with surface waters in a tidally active setting. The Central Duplin transects provided subsurface pore fluid interaction at a direct marsh-island intersection. Thick, more developed marsh systems may influence the zone of discharge and horizontal fluid migration in the shallow pore space. Although we were unable to use our resistivity measurement as a quantitative measure of fluid flux or discharge, it has provided qualitative data that shows the shallow marsh is a dynamic exchange zone. Future measurements at both sites should extend further into the river channel and couple the resistivity measurements with pore fluid water chemistry.

APPENDIX C

Grain Size Analysis:

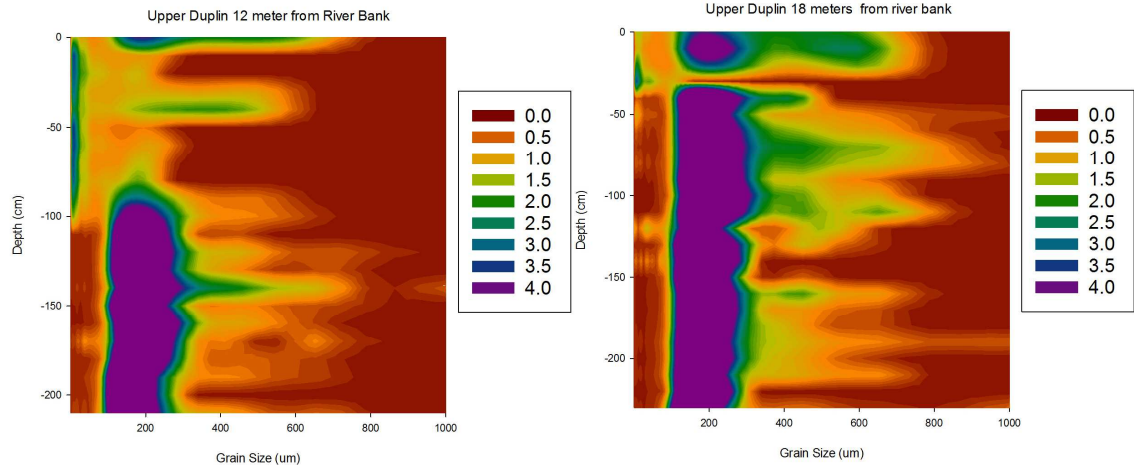
A Shallow grain size analysis was conducted on the 6 cores taken from Sapelo Island marsh transects. The separation of the data was split into geographic zones of Upper Duplin, Central Duplin, and Lower Duplin and labeled by distance from the main river channel. Results are presented in color contour figures based upon grain size at 10cm sections using a laser particle analyzer. The scales represent the particle size in percent ranging from zero (red) to greater than 4 (purple). All sales are uniform in for figures

1.1 Upper Duplin 12 meter form River Bank

The Upper Duplin low marsh core was 210 cm in length with a clear two layer system. The grain size distribution in the top 100 cm consisted of poorly sorted medium and coarse grain silts and fine to medium sands. The consistency of the material was dark rich organic marsh mud. The larger particles were most likely an artifact of organic material. Below 100 cm there was a clear transition to well-sorted fine to medium grain sands.

The Upper Duplin high marsh core was 240 cm in length with a clear two layer system. The grain size distribution in the top 40cm was poorly sorted medium and coarse silts, fine and medium sands, and organic material. The visual consistency was dark rich organic marsh mud. The larger particles seen in the plot are a result of the high organic

content within the sample. The remaining core content was well sorted medium and fine grain sands with a clear transition at 50 cm.

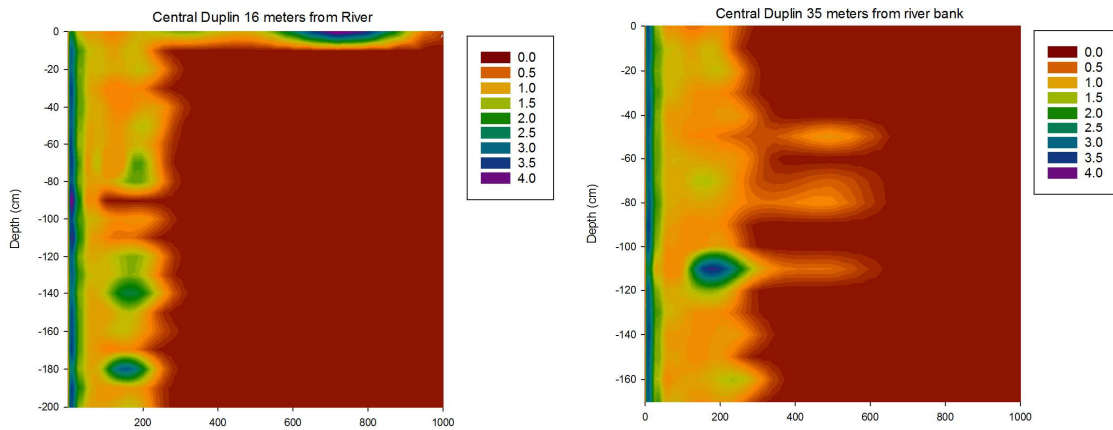


Both cores exhibited similar grain size distribution, the low marsh core that was closest to the river channel was composed of a larger over top marsh mud layer. The upper marsh core closest to the upland of Upper Duplin had a thinner marsh layer that consisted of larger particles.

2.1 Central Duplin

The Central Duplin low marsh core was 210 cm in length and was uniform in sediment material consisting of very fine to fine silts with limited fine sands. There were 3 samples at 70 cm, 140 cm, and 180 cm that had larger materials, but they are most likely associated with organic material interference. The average grain size was uniform throughout the core. The Central Duplin high marsh core was 180 cm in length and was uniform in sediment material. The majority of material was very fine to fine silts with

limited fine sands. There was one sample at 110 cm that had larger contribution of fine grain sand size material.



Both cores exhibited similar grain size distribution. The large grain size anomaly at 110cm in the upper marsh core and at 180cm in the lower marsh core may be representative of a historical sandy layer in the system.

3.1 Lower Duplin

The Lower Duplin cores were taken at 50 and 100 meters from the river channel. At this site, the marsh extended .2 km from the upland to the river channel. The low marsh core was taken 50 meters from the river in a zone that was dominated by *Spartina*. The core showed a uniform sediment type consisting of very fine to fine silts with limited fine sands intermittent. At 190 cm there was the beginning of a transitional sand layer that was beneath 10cm layer of oyster material. The upland core was taken 100 meters from the river channel in a zone dominated by *S. virginica*. The majority of the material was well sorted very fine to fine silts with limited fine sands. The entire core was

uniform in sediment type of dark organic rich marsh mud. Both cores exhibited similar grain size distribution.

